JACS
JOURNAL OF THE AMERICAN CHEMICAL SOCIETY
pubs.acs.org/JACS
Article

Methanol Synthesis from CO_2/CO Mixture on Cu−Zn Catalysts from Microkinetics-Guided Machine Learning Pathway Search

Yun-Fei Shi, Pei-Lin Kang, Cheng Shang,* and Zhi-Pan Liu*

Cite This: J. Am. Chem. Soc. 2022, 144, 13401−13414
Read Online

ACCESS | Metrics & More | Article Recommendations | Supporting Information

ABSTRACT: Methanol synthesis on industrial Cu/ZnO/Al_2O_3 catalysts via the hydrogenation of CO and CO_2 mixture, despite several decades of research, is still puzzling due to the nature of the active site and the role of CO_2 in the feed gas. Herein, with the large-scale machine learning atomic simulation, we develop a microkinetics-guided machine learning pathway search to explore thousands of reaction pathways for CO_2 and CO hydrogenations on thermodynamically favorable Cu−Zn surface structures, including Cu(111), Cu(211), and Zn-alloyed Cu(211) surfaces, from which the lowest energy pathways are identified. We find that Zn decorates at the step-edge at Cu(211) up to 0.22 ML under reaction conditions with the Zn−Zn dimeric sites being avoided. CO_2 and CO hydrogenations occur exclusively at the step-edge of the (211) surface with up to 0.11 ML Zn coverage, where the low coverage of Zn (0.11 ML) does not much affect the reaction kinetics, but the higher coverages of Zn (0.22 ML) poison the catalyst. It is CO_2 hydrogenation instead of CO hydrogenation that dominates methanol synthesis, agreeing with previous isotope experiments. While metallic steps are identified as the major active site, we show that the [−Zn−OH−Zn−] chains (cationic Zn) can grow on Cu(111) surfaces under reaction conditions, which suggests the critical role of CO in the mixed gas for reducing the cationic Zn and exposing metal sites for methanol synthesis. Our results provide a comprehensive picture on the dynamic coupling of the feed gas composition, the catalyst active site, and the reaction activity in this complex heterogeneous catalytic system.

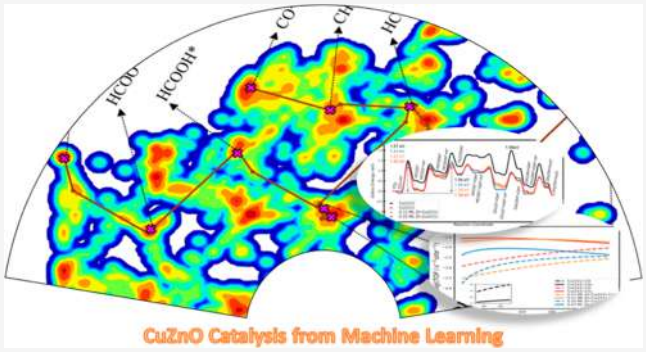

Downloaded via FUDAN UNIV on July 28, 2022 at 01:26:03 (UTC).
See https://pubs.acs.org/sharingguidelines for options on how to legitimately share published articles.

1. INTRODUCTION

Methanol synthesis that converts mixed C1 gas (CO_2, CO) and H_2 to methanol is a key industrial process for C1 utilization and of particular importance for realizing carbon neutralization. The best industrial catalyst to date, Cu/ZnO/Al_2O_3 (CZA) ternary composite catalyst,[1] is made by coprecipitation that leads to Cu−Zn containing nanoparticles (5−10 nm, Cu/Zn = 7:3 M ratio) supported on the structural promoter Al_2O_3.[1,2] The reaction is operated at high-temperature and high-pressure conditions, for example, 220−280 °C and 50−100 bar, with a mixture of CO and CO_2 as the feed gas, where the presence of CO_2 can enhance the turn-over-frequency (TOF) rate of CH_3OH formation by 2−4 times.[3−6] The past 60 years have seen significant efforts to characterize the catalyst structure and determine the reaction mechanism.[7−10] However, owing to the complexity of the multielement (Cu−Zn−Al−O) catalyst and the huge reaction network, there are still many long-standing puzzles, especially, on two key issues, namely, the role of Zn in the catalyst and the role of CO_2 in the reactant, which are central for clarifying the active site and the reaction kinetics.

Two different models of the active site are the most popular to explain the Cu−Zn synergetic effect in CZA catalysts: (i) a composite model of the ZnO_x/Cu interface[10,11] and (ii) a metal alloy model of the CuZn (surface) alloy.[9,12] While the two models differ in the geometric position and oxidation state of Zn, both of them suggest the intimate contact of Cu and Zn with strong interaction, as implied by the coprecipitation synthetic procedure. For the composite model, the major supporting evidence is the observed graphitic-like ZnO overlayer on the surface of Cu nanoparticles after catalytic reaction using high-resolution transmission electron microscopy,[10,11,13] which suggests the presence of a strong metal-support interaction of the catalyst composite. By using density functional theory (DFT) calculations and kinetic Monte Carlo (kMC) simulation, Kattel et al.[14] found a high TOF, 9.0 × 10^{-2} s^{-1}, for methanol synthesis from CO_2 hydrogenation on a manually constructed $Zn_6O_7H_7$/Cu(111) composite model. The activity is further shown to be much higher than that on a 0.11 monolayer (ML) Zn-decorated Cu(211) (Zn replacing

Received: June 8, 2022
Published: July 18, 2022

© 2022 American Chemical Society

https://doi.org/10.1021/jacs.2c06044
J. Am. Chem. Soc. 2022, 144, 13401−13414

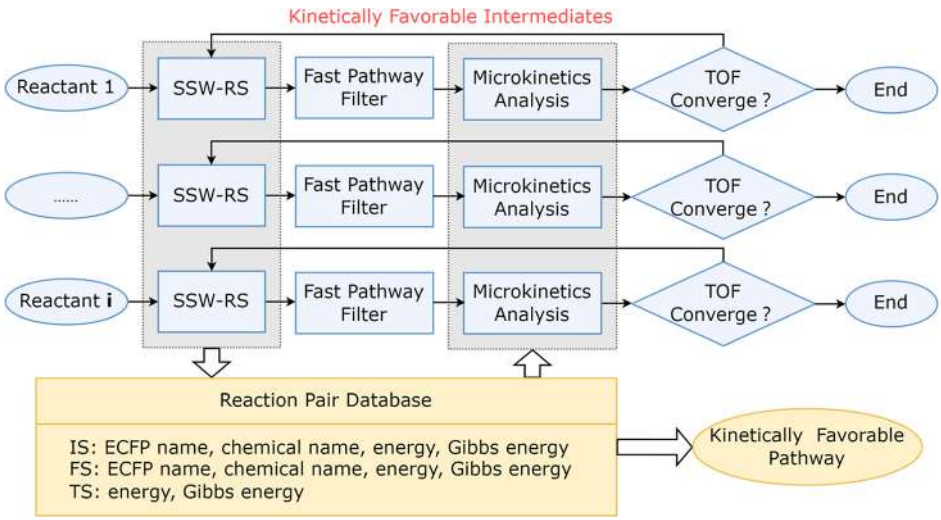

Figure 1. Scheme of MMLPS to explore the reaction network and find the reaction pathway for CO_2 and CO hydrogenation. The MMLPS simulations start by initiating a series of SSW-RS parallel runs, each branch with a distinct reactant i. The SSW-RS will continuously produce reaction information that are collected in a Reaction Pair Database. Based on the database, each branch performs the fast pathway filter to identify the kinetically most favorable intermediate, which is selected as the new reactant for the next cycle of SSW-RS. Then, each branch takes microkinetics analysis to obtain the formation rate of the target product. The branch ends if the formation rate converges, otherwise proceeds to the next cycle of SSW-RS.

the Cu at step-edge). On the other hand, the CuZn alloy model also receives strong support from thermodynamics calculations[12] and experiment:[9,12,15,16] CuZn surface alloy can form under in situ reaction conditions due to the reductive ability of CO and H_2, and there is a correlation between the Zn surface coverage and experimental activity. For example, using a Zn-deposited Cu(111) model catalyst, Nakamura et al. reported that the TOF of CO_2 hydrogenation to methanol reaches a maximum of 2.7×10^{-2} s^{-1} at 0.19 ML Zn coverage (about 10 times faster than that without Zn), where the surface Zn appears to be largely in the metallic state at a coverage lower than 0.19 ML according to the ultrahigh vacuum (UHV) XPS signal.[17] It should, however, be noticed that the higher activity of the CuZn alloy phase than the pure Cu phase cannot be confirmed from theory. Although there were some claims of high activity of CuZn alloys from DFT calculations,[10,18,19] they were later rejected by microkinetics simulations[19,20] based on DFT kinetics data.

In addition to the debate on the active site, the role of CO_2 appears to be more intriguing. While CO was initially believed to be the carbon source of methanol,[3,8] the isotopic labeling experiments[5] on commercial CZA confirm that carbon of CH_3OH product comes dominantly from CO_2 (>70%), even though CO is up to 50 times of CO_2 in the feed gas.[19,21,22] This important observation is, however, not well rationalized from theory, not least because of the great difficulty to identify the lowest energy pathway in complex systems. Apparently, to date, microkinetics simulations based on DFT energetics from different groups do not agree with each other. For example, van Rensburg et al.[20] showed that the independent CO hydrogenation is 3 orders of magnitude faster than the independent CO_2 hydrogenation, while in the combined CO and CO_2 hydrogenation, the CO_2 selectivity wins over, but the overall rate is incorrectly lower than the independent CO hydrogenation. They found that the catalyst is poisoned by the adsorbed formate (HCOO*). By contrast, Yang's group[23,24] with similar theoretical setups and models showed different results that appear to better agree with experimental facts. The independent CO_2 hydrogenation has a reaction rate similar to CO hydrogenation, although both are slow (TOF < 1×10^{-5} s^{-1}). In the mixed gas hydrogenation, CO_2 selectivity is promoted more markedly than CO selectivity, reaching the TOF of about 3×10^{-5} s^{-1}. They suggested that the precovered HCOO* now promotes CO_2 hydrogenation by reducing the reaction barrier of key elementary steps (HCOOH* to H_2COOH*) in contrast to the conclusion of van Rensburg et al.[20] Nevertheless, the rate from their results, 7.9×10^{-4} s^{-1}, is still orders of magnitude lower than that measured from experiments performed on Cu-based catalysts at the same condition (e.g., TOF estimated to be 1.7×10^{-2} to 1.7 s^{-1} on Cu/SiO_2 with the active site concentration varying from 100 to 1%, at 573 K, total pressure 13.4 bar, $p_{CO}/p_{CO_2}/p_{H_2}$ = 1:4:15).[25]

Obviously, the two issues in CZA catalysis, namely, the Zn promotion and the CO_2 enhancement, are strongly coupled with each other in kinetics. It is of great challenge to establish a comprehensive and self-consistent picture to reconcile all existing puzzles in the field. Novel approaches to treat simultaneously the variance in both the active site structure and the catalytic reaction pathway are highly desirable in the field.

Herein, we develop a microkinetics-guided machine learning pathway search (MMLPS) approach to explore the reaction network of CO_2 and CO hydrogenations and evaluate quantitatively the reaction rates on different Cu and CuZn alloy surfaces. Our MMLPS relies on a five-element Cu−Zn−C−H−O global neural network (G-NN) potential for fast potential energy surface (PES) evaluation, stochastic surface walking (SSW) reaction sampling (SSW-RS) for revealing unknown pathways, and a fast microkinetics solver to guide the pathway search. Not only the thermodynamics of various Cu−Zn structures, including different Cu, CuZn, and ZnOH-covered Cu surfaces, are resolved, the mechanism of CO and CO_2 hydrogenation is also determined. Our results shed important insights into the role of Zn and CO/CO_2 feed gas ratio on the catalyst structure and methanol synthesis activity.

https://doi.org/10.1021/jacs.2c06044
J. Am. Chem. Soc. 2022, 144, 13401−13414

2. METHODS

2.1. MMLPS Method. Our MMLPS method aims to resolve a complex catalytic network with many likely intermediates at various surface coverages in an automated way as that encountered for CO_2 and CO hydrogenations on surfaces. The MMLPS method is developed upon the SSW-RS method[26−28] (see Supporting Information, Section 1.1 for more details on the SSW-RS method), which has been successfully applied to gas-phase single-molecule reactions (e.g., glucose pyrolysis[26]) and heterogeneous reactions with two reactants[28,29] [e.g., CO + H_2O on Cu(111), water−gas-shift reaction.[28] The MMLPS method with the ability to treat a much more complex reaction network has two key features: (i) massively parallel SSW-RS simulations to consider reactions with different compositions (e.g., different coverages); (ii) automatic identification of the kinetically favorable pathways via on-the-fly microkinetics-based rate analysis. In the MMLPS method, all likely reaction patterns are generated through the SSW-RS, which are different from the conventional reaction mechanism generation approaches using specifically designed rules based on the bond matrix[30−34] (e.g., RMG,[30,31] RING,[32] pReSt[33]). The SSW-RS simulation, also unlike other pathway sampling methods such as metadynamics,[35−37] transition path sampling,[38] and discrete path sampling,[39] does not need a priori knowledge on the reaction (e.g., collective variables to desired products) and thus allows a fully automated search of a complex reaction network when incorporated in MMLPS. The high computational cost associated with PES evaluation is now dramatically reduced with the help of G-NN potential. The flowchart of the MMLPS method is shown in Figure 1 and elaborated in the following.

The MMLPS uses the idea of divide-and-conquer to solve a complex reaction network, where the reaction pathways are explored simultaneously by starting from different intermediate states that differ in chemical species and compositions (e.g., at different surface coverages). As shown in Figure 1, an MMLPS simulation initiates many parallel SSW-RS runs, each named as an SSW-RS branch that starts from a reactant composition (e.g., CO + H_2) aiming to identify the reaction pathways initiating from this reactant composition. In each SSW-RS branch, the reaction information, including the initial state (IS), the final state (FS), and the transition state (TS), is collected and recorded in a reaction pair database (yellow box in Figure 1) shared by all SSW-RS branches, which distinguish different reactions by the name of IS and FS using the extended-connectivity fingerprints with the diameter level 4 (ECFP-4)[40] (see Supporting Information Section 1.3 for the example of ECFP-4). The database only stores the reaction pair with the lowest barrier for the same reactions with the same chemical name on the reactants. The reactions related to molecular diffusion on the surface or the surface structure reconstruction (e.g., Zn−Cu atom swap) are not considered in the reaction pair databases because the former is generally fast and non-rate-determining, and the latter decouples generally from catalytic reactions and, if occurs, reflects correctly the heterogeneous surface status during the reaction.

Each SSW-RS branch is controlled by an independent microkinetics module, which is implemented to facilitate on-the-fly reaction pathway analyses. The microkinetics module is to identify an unexplored intermediate associated with low-energy pathways that is then taken as the starting state in the next cycle of SSW-RS (red arrows in Figure 1). The low-energy reaction pathways are first screened using the so-called "circuit reaction theory." The theory is rooted in microkinetics theory, which regards the reaction network as an analogy to the electrical circuit (also see the recent work by Hu group[41] and early publications[42−46]). By mathematical derivations, it can be shown that the steady-state microkinetics follows the Ohm law of a circuit (see Supporting Information Section 1.4 for the detailed derivation), where each elementary reaction is analogous to resistance and the rate is then the current. The lowest energy pathway, the one equivalent to the branch with the lowest resistance in the circuit, can be then identified using the graph theory.

Here, we briefly describe the method to evaluate the resistance of a pathway. To be general, for an elementary reaction k with several surface adsorbates on the surface, the TS of the reaction can be considered to contain a TS complex ($\neq$), a number of spectating (nonreacting) adsorbates (j = 1, ...), and free surface sites (*). As shown in Supporting Information Section 1.4, the resistance R_k for an elementary reaction k can be computed using eq 1

$$R_k = \exp\left(\frac{\mu_{\neq} + \sum_j \mu_j - n_* \mu_*}{k_b T}\right) \tag{1}$$

$$\mu_i = \mu_i^0 + k_b T \ln(\theta_i) \tag{2}$$

where $\mu_{\neq}$, μ_*, and μ_j are defined to be the "chemical potential" of the TS complex, free site, and the spectating adsorbate j, respectively; n^* is the number of free sites taking part in the reaction. μ_i (i represents the adsorbate j or *) can be further computed using eq 2 by using the coverage-independent Gibbs free energy μ_i^0 ($\mu_*^0 = 0$ by definition) and its coverage θ_i at the steady state. It should be noted that the steady-state coverages must be solved iteratively to achieve the reaction balance, which is nontrivial for a complex reaction network. Finally, the total resistance for a single pathway with a sequence of elementary reactions can be obtained from eq 3.

$$R_{\text{path}} = \sum_k^{\text{path}} R_k \tag{3}$$

The circuit theory can elegantly evaluate the resistance of a pathway, even when the pathway does not end properly (mimicking an open circuit), which is useful when the reaction pair database is not complete yet.

To speed up the microkinetics analysis, the microkinetics module utilized in MMLPS is performed via two stages in two submodules, namely, the fast pathway filter and the microkinetics analyzer. These two submodules are further described in the following.

(a) Fast pathway filter. This step is for fast screening of the best pathway candidates from a complex reaction network. To do so, the resistance of a pathway can be approximately calculated using $R'_{\text{path}} = \sum R'_k$, where the approximated total resistance R'_k is computed using eq 4. Comparing eqs 4 with 1, the steady-state coverage term in eq 2 is neglected, and $\mu_{\neq}^0 + \sum_j \mu_j^0$ is, in fact, the free energy of the TS, G_{TS}.

$$R'_k = \exp\left(\frac{\mu_{\neq}^0 + \sum_j \mu_j^0}{k_b T}\right) = \exp\left(\frac{G_{\text{TS}}}{k_b T}\right) \tag{4}$$

G_{TS} is referenced to the initial reactant and can be derived from the total energy (G-NN level in this work) in the reaction pair database with appropriate corrections to free energy. In this work, we set the gas-phase molecules CO_2, CO, H_2, CH_3OH, and H_2O at 500 K and pressure 10, 10, 40, 1, and 1 bar, respectively, under typical industrial conditions for the free-energy correction of gas-phase molecules (see Supporting Information Section 2.1 for more information).

With the resistance value for each elementary reaction, we can use the graph algorithms, namely, Yen's algorithm[47] for the k-shortest paths based on Dijkstra's algorithm,[48] to search for the lowest-energy pathway to every intermediate. All pathways are ranked according to the total resistance of the pathway. The top pathway with the lowest resistance that contains a new intermediate can then be identified, and this new intermediate is selected as the starting reactant in the next cycle of the current SSW-RS branch (red arrows in Figure 1). The current SSW-RS branch will be terminated if no further new intermediates with a low barrier to access (e.g. <2 eV) can be found at the current composition.

(b) Microkinetics analyzer. Every time a certain SSW-RS branch finishes one cycle, we need to merge the individual network into a whole network to run the microkinetics analyzer module. The merging process will align reactions from different sub-branches to the same chemical composition by augmenting or subtracting the gas-phase free energy of the reactants to keep the mass balance, which is

https://doi.org/10.1021/jacs.2c06044
J. Am. Chem. Soc. 2022, 144, 13401−13414

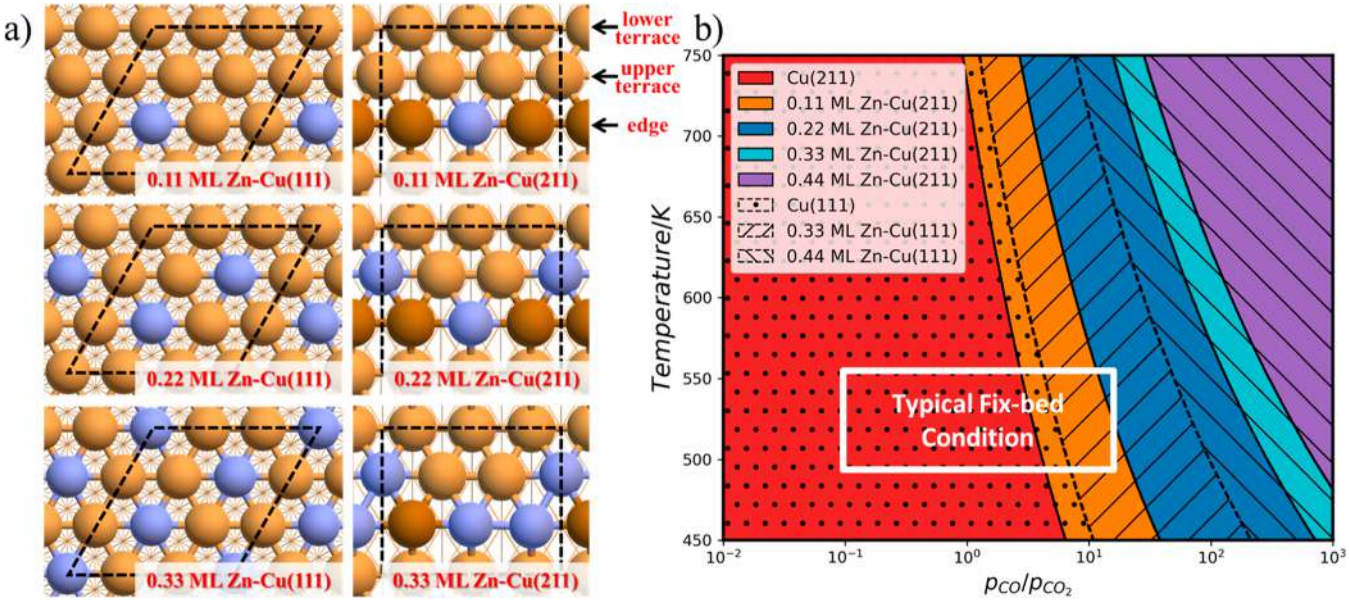

Figure 2. (a) Most stable structures for Zn-alloyed Cu(111) and Cu(211) surfaces from SSW-NN global search. Black dash indicates the supercell. Color scheme of atoms: Cu, yellow; Zn, blue; edge Cu, brown. (b) Thermodynamics phase diagram of Zn-alloyed Cu(111) and Cu(211) surfaces. The thermodynamics stability of the surface at various temperatures and CO/CO_2 pressures (p_{CO}/p_{CO_2}) is described by the formation free energy $\Delta G_{CuZn}(T,p)$, explained in Supporting Information Section 3. Color area for (211) and shaded area for (111) are overlapped in one plot, which shows that (211) forms surface alloys at lower temperatures and p_{CO}/p_{CO_2} ratios.

detailed in Supporting Information Section 1.2. From this merged reaction network, the top-ranked pathways (e.g., maximally 20 pathways) from the reactant to the target product, if present (e.g., from CO_2 + $3H_2$ to CH_3OH + H_2O), are determined. With these pathways, we build a full microkinetics model to compute the steady-state rate, where the species coverages are now determined explicitly. The ordinary differential equations of all reactions are solved using the backward differentiation formula method,[49] and the solution is further polished by Newton's method optimization.[50] If the rate does not change after a certain number of SSW-RS cycles, this branch of SSW-RS is terminated. The MMLPS simulation stops when all SSW-RS branches have exited.

2.2. G-NN Potential Calculations. A five-element Cu−Zn−C−H−O G-NN potential is utilized to speed up the reaction sampling in the methanol synthesis on CuZn alloys. This dataset for training inherits the global datasets utilized previously for Cu−C−H−O and Zn−O−H G-NN potentials[28,51,52] and add new datasets from the Cu−Zn−C−H−O global PES. The G-NN potential is generated by the SSW-NN method in the LASP program,[53] which provides a powerful platform for iterative self-learning of the global PES from SSW.[54] The G-NN generation using the SSW-NN method has been described previously,[54,55] and the procedure is detailed in Supporting Information Section 4 as well.

The final global dataset for Cu−Zn−C−H−O contains 63539 structures, and the NN architecture for each element has a four-layer feed-forward 373-50-50-1 architecture, 373 power-type structure descriptors for the first input layer, and 2 hidden layers, each containing 50 nodes with the hyperbolic tangent activation function. The G-NN potential is available from the LASP website (www.lasphub.com). The root-mean-square error of the final NN on the whole dataset is 2.99 meV/atom and 0.080 eV/Å for energy and force, respectively. The dataset description is described in Supporting Information Section 4 together with the benchmark between G-NN and DFT calculations for the reaction pairs sampled.

2.3. DFT Calculations and Choice of DFT Functional. All DFT calculations are performed by using plane-wave DFT code, VASP,[56] where the electron−ion interaction is represented by the projector augmented wave pseudopotential.[57] The exchange functional generalized gradient approximation Perdew−Burke−Ernzerhof (PBE)[58] is used for training dataset generation as well as validation, and the kinetic energy cutoff is 450 eV. The first Brillouin zone *k*-point sampling utilizes the Monkhorst−Pack scheme with an automated mesh determined by 25 times the reciprocal lattice vectors (1/Å). Grimme's D3 method (DFT-D3) is taken to correct the van der Waals (vdW) interaction. The energy and force critera for convergence of the electron density and structure optimization are set at 5×10^{-6} eV and 0.05 eV/Å, respectively. The TS is located by the double-ended surface walking method, which is further verified by vibrational frequency calculations and structure extrapolation from the located TS to the neighboring minima. It should be emphasized that, if not explicitly mentioned, all energetics reported in this work are from DFT calculations by reconverging the low-energy G-NN structures.

The choice of DFT functional is known to affect the energetics in the reaction profile and thus change the reaction kinetics.[59] In this work, we utilize the widely used PBE-D3 functional for treating catalytic reactions on Cu−Zn surfaces. In the literature, BEEF-vdW[60] functional is another popular choice for investigating the methanol synthesis on Cu.[18,19,23,24] However, we note that the H atom (H*) adsorption energy is predicted to be −0.11 eV on Cu(111) using BEEF-vdW with respect to the gas-phase H_2,[18] while it is slightly larger, −0.24 eV, using PBE-D3, which is closer to the experimental result of −0.3 to 0.4 eV.[61] Meanwhile, the enthalpy changes for gas-phase reactions $CO_2(g) + 3H_2(g) \rightarrow CH_3OH(g) + H_2O(g)$ and $CO(g) + 2H_2(g) \rightarrow CH_3OH(g)$ are predicted to be −0.50 and −1.36 eV by the PBE-D3 functional and those from the BEEF-vdW functional are 0.00 and −0.82 eV, respectively. Although both functionals are not good enough when compared with the experimental values (−0.55 and −0.98 eV), the PBE-D3 functional appears to provide a better description for CO_2 hydrogenation, the major reaction channel known from the experiment. To reproduce the experimental thermodynamics in our microkinetics analyses, we adopt −0.44 and −0.05 eV corrections for gas-phase CO and CH_3OH free energies (cf. the energy of CO_2 and H_2 are corrected by +0.33 and +0.09 eV when BEEF-vdW functional is used[18]). More details on the influence of the accuracy of reaction energetics on kinetics can be found in Supporting Information Section 2.2.

https://doi.org/10.1021/jacs.2c06044
J. Am. Chem. Soc. 2022, 144, 13401−13414

3. RESULTS

3.1. Thermodynamics of CuZn Surface Alloy. In order to establish a valid surface model, we here revisit the structure of the CuZn surface alloy under the catalytic conditions, focusing on the coverage and the position of Zn. With SSW-NN global optimization to explore exhaustively the stable structure candidates, we are now able to examine in detail the thermodynamics tendency in forming CuZn surface alloy under reaction conditions. The close-packed terrace Cu(111) and monoatomic stepped Cu(211) surface are utilized as the model catalyst where the Zn coverage is varied from 1/9 (0.11) to 4/9 (0.44) ML (with respect to exposed metal atoms). A series of SSW-NN simulations are carried out with Zn randomly replacing Cu on the surface or in the bulk initially. At least 10000 minima for each coverage are visited by SSW-NN, from which the global minima (GM) at different Zn coverages are identified. In total, we identify 1808 unique surface alloy structures after removing the duplicates by using the distance-weighted Steinhardt-type order parameter[62] as the structure fingerprint. As depicted in Figures 2a and S6 for all GM structures, we found that Zn atoms strongly prefer to expose on the surface, and importantly, the Zn−Zn metallic bond is not present until a coverage above 0.33 ML for Cu(111) and 0.22 ML for Cu(211).

From the energetics of the GM structures, Figure 2b plots the thermodynamics phase diagram of the CuZn surface alloy on (211) and (111) surfaces, respectively, at different O chemical potentials, μ_O, by referencing Cu metal and ZnO bulk oxide. μ_O can be derived as a function of temperature and relative pressure p_{CO}/p_{CO_2} from the chemical formula of CO oxidation as detailed in Supporting Information Section 3. From Figure 2b, we find that the reductive gas CO can indeed transform ZnO to Zn in forming CuZn surface alloy on both stepped Cu(211) and Cu(111) terraces, as shown by the red box that indicates the typical reaction conditions. The ZnCu alloy preferentially forms at the Cu step-edge at relatively low CO pressures and becomes thermodynamically feasible at Cu terraces at higher CO pressures.

As shown in Figure 2b, on going to a higher ratio of p_{CO}/p_{CO_2} where μ_O gets lower, the Zn surface coverage increases gradually. The temperature plays a less important role in affecting the Zn coverage. At the typical fix-bed industrial methanol synthesis condition, that is, 500−550 K, p_{CO}/p_{CO_2} = 0.1−20 (the white box in Figure 2b) up to 0.22 ML on (211) step and 0.33 ML on (111) terrace are thermodynamically stable, indicating that pure Cu surface without or with low coverage of Zn is the major metallic component in CZA catalysts. Even under the extreme reduction condition (∼550 K, p_{CO}/p_{CO_2} = 100), we find that the Zn coverage is still no more than 0.33 ML on (211). Specifically, for the (211) surface, when p_{CO}/p_{CO_2} is less than 2.6 and the temperature is low (500 K), no Zn is present (ZnO is preferred), and at the higher temperature (>525 K) and the high p_{CO}/p_{CO_2} ratio (p_{CO}/p_{CO_2} > 7.8), 0.22 ML Zn, namely 0.22 ML Zn−Cu(211), will be the most stable.

By inspecting closely at the GM structures (Figure 2a), we noticed that in all GM structures, Zn atoms occupy the original position of surface Cu atoms and can appear at both terrace and step positions. For the (111) surface, the thermodynamically allowed 0.33 ML Zn−Cu(111) (Figure 2a) has the $p(\sqrt{3} \times \sqrt{3}R30°)$ surface patterns with Zn separated from each other. For the (211) surface, the first 0.11 ML Zn prefers to stay at the edge of the (211) step, which is at least 0.05 eV more stable than the upper terrace near the edge and 0.15 eV more stable than the lower terrace underneath the step (see Figure 2a). Furthermore, the subsurface and bulk Zn are considerably less stable (>0.25 eV), indicating the strong tendency of Zn enrichment on the surface. Increasing to 0.22 ML Zn coverage, the newly added 0.11 ML Zn prefers the (111) upper terrace, one lattice away from the initial 0.11 ML Zn at the step-edge (see Figure 2a). Apparently, the Zn-segregated configuration with Zn−Zn bonds is less favorable by 0.03 and 0.06 eV for both Zn at the step-edges and the upper terraces, respectively.

Similarly, the GM for 0.33 ML Zn−Cu(211), although being thermodynamically unfavorable at the reaction conditions (outside the white box), has 0.22 ML Zn at the edge and 0.11 ML Zn at the terrace. The fully Zn-decorated Cu(211) is less stable (by 0.07 eV) than this GM and much less stable (by 0.31 eV) than 0.22 ML Zn−Cu(211) at the reaction condition (500 K, p_{CO}/p_{CO_2} = 1). Our results suggest that the Zn−Zn dimeric structure in the Cu matrix is thermodynamically unlikely under catalytic conditions. Instead, the local structure pattern from 0.22 ML Zn−Cu(211), that is, with 0.11 ML Zn at the edge and 0.11 ML at the nearby upper terrace Zn (Figure 2a), should be a dominant structure pattern at Cu monoatomic steps.

We may emphasize that the previous works considered only limited numbers of likely configurations at selected Zn coverages for modeling CuZn surfaces. For example, the fully Zn-decorated Cu(211) edge utilized by Kuld et al.[12] and Studt et al.[19] to model CuZn catalysis, although simplifies largely the reaction modeling, is not the thermodynamically favorable surface pattern in CZA catalysts from our results. The global structure exploration as utilized in this work via SSW-NN can better capture the stable surface structures under reaction conditions.

3.2. Reaction Database and Pathways from MMLPS. By using MMLPS, we then investigate catalytic reactions starting from different reactant compositions up to two carbon atoms, including CO_2 + H_2, HCOOH + H_2, HCHO + H_2, HCOO* + CO_2 + H_2, and HCOO* + HCHO + H_2, on three stable surfaces relevant to the catalytic conditions, that is, Cu(211), 0.11 ML Zn−Cu(211), and 0.22 ML Zn−Cu(211). The compositions with two carbon atoms, for example, HCOO* + HCOOH + H_2, are also considered to investigate the possible kinetics influence of coadsorbed species, particularly the adsorbed format HCOO*. For comparison, Cu(111), the known poor catalyst for methanol synthesis,[10,63,64] is also investigated using MMLPS, starting from CO_2 + H_2, HCOOH + H_2, and HCHO + H_2 compositions.

It should be emphasized that MMLPS can sample simultaneously a great number of minima and the reactions in between them. For example, the MMLPS simulation for C1 reactions on Cu(211) visits 1,220,000 minima in total, which are collected from three branches of SSW-RS, that is, CO_2 + H_2, HCOOH + H_2, and HCHO + H_2, with 61 cycles in total and 20,000 minima for each cycle. This leads to a total of 14,958 reaction pairs, ∼1.2% efficiency in finding reactions. By keeping the lowest barrier one, we finally obtain 372 unique elementary reactions with 115 unique intermediates that are stored in the reaction dataset for CO_2 and CO hydrogenation

https://doi.org/10.1021/jacs.2c06044
J. Am. Chem. Soc. 2022, 144, 13401−13414

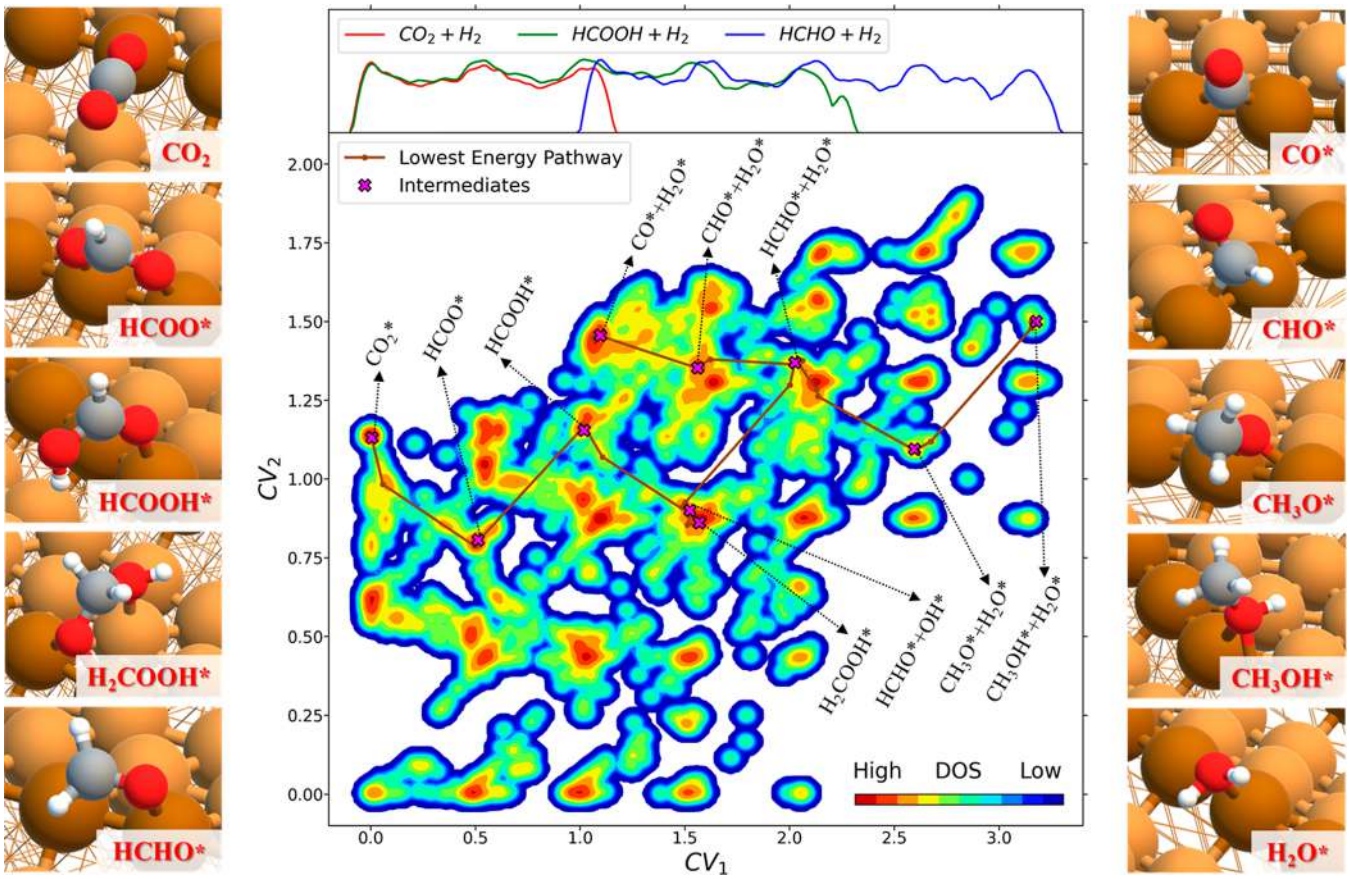

Figure 3. Contour plot for 14958 reaction pairs (IS, TS, and FS) from the low-energy pathways obtained by MMLPS on Cu(211). The color indicates the density of state reflecting the occurrence frequency of the state in the reactions. The intermediates along the lowest-energy pathway (IS, TS, and FS) are highlighted by brown lines, and their optimized geometries in GM are shown on the side panels, where the color scheme for atoms is as follows: C: gray; H: white; O: red; terrace Cu: yellow; step-edge Cu: brown. Purple crosses indicate the GM of intermediates. H (H_2) is omitted in all formulas. Structures of the coordination function-based collective variable are designed to distinguish the states (CV_1 and CV_2), with the equations shown in Supporting Information Section 6.

on Cu(211). Table S4 summarizes the reaction database obtained from MMLPS simulation for Cu(211) as the example, which includes the cycle number of SSW-RS, the total number of minima visited, the total number of reaction pairs collected, the number of unique species, and the number of unique reactions after deleting the redundant information.

To better illustrate the reaction data, we select 14958 reactions from low-energy pathways on Cu(211) obtained from MMLPS and project them into a 2D figure in Figure 3. The *x*-axis and *y*-axis of the figure are the collective variables (CV_1 and CV_2)[36] designed to distinguish different reaction intermediates, including IS, TS, and FS of reaction pairs (the equation of CV can be found in Supporting Information Section 6). The color of the map indicates the density of the intermediate states: the higher the density of the intermediate, the more frequent the intermediate is encountered in the reaction data. The insets on the top axes are the one-dimensional projection for the source-distinguished density of the intermediates, that is, red curve from CO_2 + H_2, green from HCOOH + H_2, and blue from HCHO + H_2. Obviously, CO_2 + H_2 mainly covers the left-bottom part of the figure, and by combining data from all three sources, the whole map is established, reflecting the power of the divide-and-conquer in completing the complex reaction network.

We label 10 high-density minima frequently encountered in SSW-RS simulation using the purple-cross symbols. We note that these intermediates are indeed the key intermediates well discussed in the literature for methanol synthesis including CO_2, HCOO*, HCOOH*, H_2COOH*, CO*, CHO*, HCHO*, CH_3O*, and CH_3OH. In general, the less frequently visited minima are often either thermodynamically less stable or kinetically less favorable compared to their neighboring minima with close geometry, such as COOH*, H_2COO*, $HC(OH)_2$*, $H_2C(OH)_2$*, HCOH*, COH*, CH*, CH_2*, CH_3*, and CH_4*.

Based on this reaction database, the microkinetics module in MMLPS is then utilized to identify the lowest-energy pathway to the target product, CH_3OH. Not surprising, our results for the lowest-barrier pathway are consistent with those reported in the literature.[10,19,23,64] On all surfaces investigated, the reaction mechanism from the lowest-energy pathway is the same, namely, CO_2 hydrogenation following the formate pathway via CO_2−HCOO*−HCOOH*−H_2COOH*−HCHO*−CH_3O*−CH_3OH*−CH_3OH and CO hydrogenation taking the formyl pathway via CO−CO*−CHO*−HCHO*−CH_3O*−CH_3OH*−CH_3OH. These pathways are linked by the solid lines in Figure 3, and the most stable configurations of these key intermediates are also shown in the side panels. Many less favorable pathways have been identified and, for their too low contributions to kinetics, are only discussed in Figure S8. For example, on Cu(211), the reaction pathways from HCHO to CH_3OH via HCHO*−CH_2OH*−

https://doi.org/10.1021/jacs.2c06044
J. Am. Chem. Soc. 2022, 144, 13401−13414

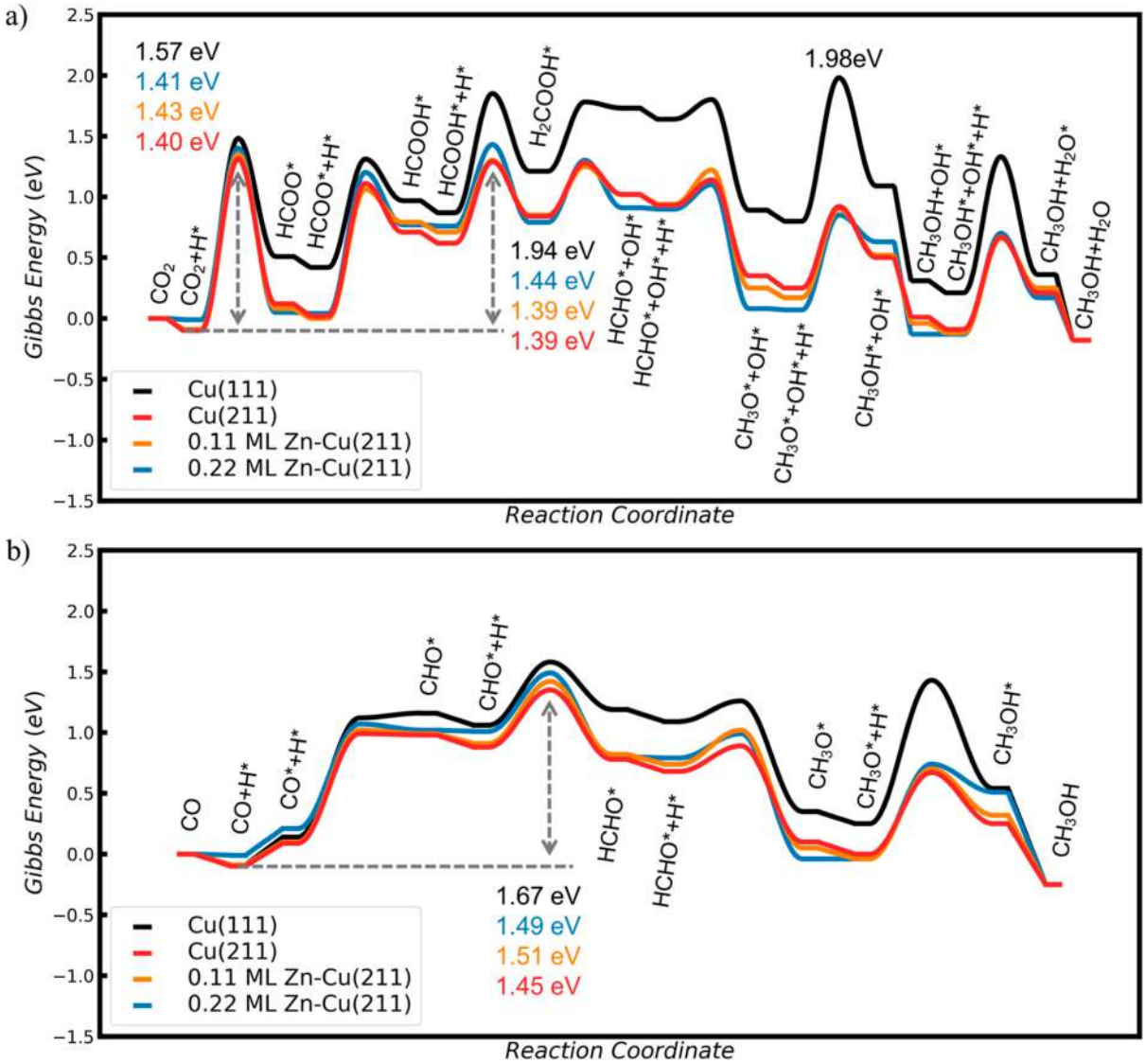

Figure 4. Gibbs free-energy profiles for (a) CO_2 hydrogenation and (b) CO hydrogenation on Cu(111) (black), Cu(211) (red), 0.11 ML Zn−Cu(211) (orange), and 0.22 ML Zn−Cu(211) (blue) at 500 K and 40, 10, 10, 1, and 1 bar of H_2, CO_2, CO, CH_3OH, and H_2O, respectively. All structures along the pathways can be found in the Supporting Information.

CH_3OH* and HCHO*−CH_2OH*−CH_2*−CH_3*−CH_3OH* are at least 0.6 eV higher than the pathway via CH_3O* (HCHO*−CH_3O*−CH_3OH*−CH_3OH, 0.93 eV) from G-NN calculations.

Considering the reaction data with two C atoms that are collected from HCOO* + CO_2 + H_2, HCOO* + HCOOH + H_2, and HCOO* + HCHO + H_2 simulations, the size of the database expands further, and thus the reaction network becomes more complex. These data represent CO_2 and CO hydrogenations on Cu(211) in the presence of another C1 species. There are 2143 unique elementary reactions and 954 unique intermediates, which are pruned from 20,978 reaction pairs and more than 2,500,000 minima visited in 6 parallel SSW-RS runs (∼0.8% efficiency in finding reactions).

From the microkinetics analysis in MMLPS with the target product being set as HCOO* and CH_3OH, we find that the formate pathway from CO_2 to CH_3OH and the formyl pathway from CO to CH_3OH are still the lowest-energy pathways: the additional C1 species does not affect the reaction mechanism. We will discuss the influence of coadsorbed HCOO* on the reaction kinetics in the next section.

3.3. Reaction Mechanisms on Cu and CuZn Surfaces.

With the reaction pathways obtained by MMLPS (G-NN calculations), we further validate and converge the low-energy pathways by DFT in order to get more accurate kinetics data. The Gibbs free-energy profiles of the reactions on different Zn-covered surfaces in the absence of HCOO* species are shown in Figure 4. The detailed data are listed in Table S5, which includes the relative (free) energy of key intermediates and TSs in the presence and absence of the spectating HCOO* species. The optimized structures, including the minima and the TS, are also included in the Supporting Information. All energies are with respect to the clean surface and the relevant gas-phase molecules, that is, CO_2, H_2, and H_2O in CO_2 hydrogenation reaction and CO and H_2 in CO hydrogenation.

It might be mentioned that we have compared our DFT energetics (PBE-D3) with the previously calculated data, as shown in Tables S6 and S7, including the work by Grabow and Mavrikakis (PW91 functional),[64] Wang et al. (optPBE-vdW

https://doi.org/10.1021/jacs.2c06044
J. Am. Chem. Soc. 2022, 144, 13401−13414

functional),[65] Sun et al. (PBE-D3),[66] and Kattel et al. (PW91 functional).[14] For the reaction barriers of eight key elementary reactions in CO_2 and CO hydrogenations, we find that the calculated barriers on Cu(111), Cu(211), and 0.11 ML Zn−Cu(211), although in different DFT functionals, agree generally well with the average deviation below 0.10 eV. There are some reactions with large deviations, which are, fortunately, kinetically less important, for example, 0.72 eV difference in CH_3O* hydrogenation between our results and the work of Kattel et al. (PW91 functional).[14] These differences are mainly caused by the TS geometry, where MMLPS utilized in this work identifies the better TS structure (see the Supporting Information for the optimized structures). In the following, we report in detail our results on Cu surfaces and Zn−Cu alloy surfaces.

Cu surfaces. On the Cu(111) surface, the key intermediates, such as CHO*, HCOO*, and H_2COOH*, are generally much less stable than those on Cu(211). As a result, the highest energy on Gibbs free-energy profile of CO_2 hydrogenation is 1.98 eV high on Cu(111), which corresponds to the TS of CH_3O* + H*, as indicated in Figure 4 black lines. For CO hydrogenation, the highest energy is 1.67 eV, which takes place at the CHO* + H* step. Both of them are much higher than those on the stepped Cu(211), suggesting the low activity of the (111) surface. Thus, in the following, we will focus on the more active Cu(211) to elaborate on the reaction mechanism.

For CO_2 hydrogenation on Cu(211) (red line Figure 4a), due to the weak adsorption of CO_2, the first step of CO_2 hydrogenation follows an Eley−Rideal mechanism in which the gas-phase CO_2 reacts with an adsorbed H* atom to produce a bidentate formate HCOO* adsorbed at the step-edge (Figure 3 and the structure shown in Figure S9). Since the reaction needs to overcome the gas-phase entropy of CO_2, it has a high free-energy barrier of 1.40 eV. The second H* then attacks one O atom of HCOO*, forming formic acid, HCOOH*, with a free-energy barrier of 1.09 eV, and HCOOH* adsorbs at the edge site through its carbonyl oxygen. The third H* reacts with the C atom of HCOOH* to generate H_2COOH* with a free-energy barrier of 0.68 eV, equivalent to 1.39 eV of the overall barrier with respect to CO_2(g) and H*. The H_2COOH* is unstable and can easily dissociate to HCHO* and OH* with a free-energy barrier of 0.44 eV. Further hydrogenation of HCHO* then creates CH_3O*, which is exothermic by 0.56 eV with a low barrier of 0.22 eV. Finally, CH_3O* is hydrogenated to CH_3OH* with a free-energy barrier of 0.67 eV, and the latter can then desorb to release 0.45 eV. The (211) surface is recovered once the remaining OH* is hydrogenated to water that leaves the surface. In summary, the CO_2 hydrogenation to formate (CO_2 + H*) and the H_2COOH* formation (HCOOH* + H*) are the two key steps with similar overall free-energy barriers on Cu(211).

For CO hydrogenation on Cu(211), the reaction starts from the adsorption of CO at the bridge site of the step-edge that is exothermic by 0.19 eV in free energy. Next, CO* reacts with H* to generate formyl CHO*, which needs to overcome a 0.90 eV free-energy barrier, and the reaction is endothermic by 0.89 eV. Since CHO* can readily return back to CO*, it needs to react immediately with another nearby H* to become HCHO*. The formation of HCHO* (CHO* + H*) is thus the key step with an overall free-energy barrier of 1.45 eV with respect to CO* and H*. The further hydrogenation steps from HCHO* to CH_3OH are identical to those in CO_2 hydrogenation.

Zn−Cu alloy surfaces. Our results show that the presence of Zn does not change the reaction mechanism of CO_2 and CO hydrogenation, as shown in Figure 4. Focusing on the key reaction steps (i.e., CO_2 + H*, HCOOH* + H*, CHO* + H*), we can find that Zn alloying slightly modifies the overall barrier but generally in the direction to increase the barrier. The overall free-energy barriers of these key reaction steps generally increase slightly in the presence of Zn. The salient features of the reactions on Zn−Cu(211) are summarized as follows.

(i) The presence of Zn increases the stability of the adsorbed HCOO* and CH_3O*, both with O-metal bondings, but weakens slightly the adsorption of other species with H-metal and C-metal bondings, such as H* and HCOOH*. The free adsorption energies of HCOO* and CH_3O* are 0.04 and 0.10 eV stronger on 0.11 ML Zn−Cu(211) than on Cu(211), and they are further enhanced by 0.03 and 0.17 eV on 0.22 ML Zn−Cu(211), respectively. On the other hand, the adsorptions of H*, HCOOH*, and H_2COOH* are weakened by 0.01, 0.08, and 0.01 eV on 0.11 ML Zn−Cu(211), respectively, and they are weakened by 0.09, 0.06, and 0.05 eV on 0.22 ML Zn−Cu(211), respectively, compared with those on Cu(211).

Interestingly, we observe the adsorbate-induced Zn−Cu exchange on Zn−Cu alloy. Because the adsorption HCOO* prefers the bidentate geometry with two O bonding with metals, it can reconstruct the (211) step-edge by forming a Zn−Zn dimer pattern in the 0.22 ML Zn−Cu(211), as shown in Figure S9c. The adsorption structure of HCOO* on the Zn−Zn dimer is, however, only 0.03 eV per HCOO* lower than that on the non-reconstructed surface (i.e., on the Zn−Cu pair). This suggests that Cu−Zn exchange under reaction conditions has been properly considered in our MMLPS and has only negligible effects on reaction profiles.

(ii) The presence of Zn generally destabilizes the TS of the key reactions. The Gibbs free energy is 0.04 eV higher for the TS of CO_2 + H*, 0.01 eV for the TS of HCOOH + H*, and 0.08 eV for the TS of CHO* + H* on 0.11 ML Zn−Cu(211) than Cu(211). The values of the three reactions change to 0.10, 0.14, and 0.14 eV on 0.22 ML Zn−Cu(211). This trend can be understood since these TSs generally involve the C-metal or H-metal bonding, as shown in Figure S9, where Cu is preferable in bonding.

The role of HCOO* spectator. Since MMLPS also maps out the reaction pathways in the presence of HCOO* spectator, we are in a position to compare systematically the free energy for CO_2 and CO hydrogenations on the surfaces in the presence of 0.11 ML HCOO* on Cu(211) and Zn−Cu(211) surfaces. The DFT energetics are also listed in Table S5, and the free-energy profiles are shown in Figure S10.

We find that even with only 0.11 ML HCOO*, not only the most adsorbed intermediates are weakened in adsorption but also the TSs become less stable, which leads to the higher barrier in the presence of HCOO* spectators. As a good example, the adsorption energy of HCOO* itself (0.22 ML) is destabilized by 0.33 eV on Cu(211), 0.35 eV on 0.11 ML Zn−Cu(211), and 0.45 eV on 0.22 ML Zn−Cu(211). This is apparently due to the fact that the first HCOO* occupies the step-edge, and thus the second HCOO* has to bond with the terrace site from 0.11 to 0.22 ML (Figure S11).

Importantly, the overall free-energy barrier of H_2COOH* formation in the presence of HCOO* spectator increases by

https://doi.org/10.1021/jacs.2c06044
J. Am. Chem. Soc. 2022, 144, 13401−13414

0.19, 0.19, and 0.14 eV on Cu(211), 0.11 ML Zn−Cu(211), and 0.22 ML Zn−Cu(211), respectively. Since the TS of HCOOH* + H* is at the highest energy position on the Gibbs free-energy profile, it implies that the spectating HCOO* is a poisoner to the CO_2 hydrogenation.

We note that the only species that becomes more stable in the presence of HCOO* spectator is the adsorbed H_2O* that gains an extra 0.50 eV in adsorption. The configuration features the formation of an H-bonding network between H_2O* and nearby HCOO* at the step-edge of (211) (Figure S11), which was ignored previously in the work of Wu and Yang.[23] We will show later that the strong adsorption of H_2O* nearby the preadsorbed HCOO* leads to high coverage of H_2O* at the steady state and thus a lower rate to methanol on 0.11 ML HCOO*/Cu(211) (Figure S14).

3.4. Microkinetics. Based on the DFT energies (all data detailed in Table S5), we then perform microkinetics simulations to evaluate the reaction rate on different catalyst surfaces. Our main results are shown in Figure 5a,b, where the calculated TOF [log(TOF)] at the steady state is plotted against the reaction temperature from 480 to 580 K. The pressures for the gas-phase CO_2, CO, H_2, CH_3OH, and H_2O are set at a typical industrial reaction condition, that is, 10, 10, 40, 1, and 1 bar, respectively. In microkinetics simulation, since all reactions occur exclusively at the step-edge of (211), the coverage refers to the effective coverage θ_i^{eff} on the step-edge sites only, while the true coverage θ_i on (211) reported below is 1/3 of θ_i^{eff}. Three key findings for CO and CO_2 hydrogenations on Cu and CuZn surfaces are thus summarized in the following.

First, as shown in Figure 5a, CO_2 hydrogenation is markedly faster than CO hydrogenation on the two most active catalysts, that is, Cu(211) and 0.11 ML Zn−Cu(211), both being the stepped sites. The stepped sites as appeared in Cu(211) are much more active than the (111) terrace by at least 3 orders of magnitude (Figure 5a inset). The computed TOF for reaction on Cu(211) at 500 K is 2.8×10^{-2} s^{-1}, which is 10 times faster than that of CO hydrogenation (2.2×10^{-3} s^{-1}). The slowest elementary step in CO_2 hydrogenation is HCOOH* + H* reaction ($r_+ = 5.1 \times 10^{-2}$ s^{-1}) at the steady-state, which is still 1 order of magnitude faster than the one in CO hydrogenation, CHO* + H* ($r_+ = 2.2 \times 10^{-3}$ s^{-1}). This difference originates not from the forward reaction barrier but from the extremely low coverage of CHO* species ($\theta_{\mathrm{CHO*}} = 4.0 \times 10^{-12}$ ML), which can readily decompose back to CO* and H*. The slower rate of CO hydrogenation is thus caused by the poor stability of CHO* intermediate on Cu surfaces compared to HCOO* and HCOOH* intermediates in CO_2 hydrogenation.

In total, 92.7% of CH_3OH comes from CO_2 at 500 K on Cu(211), and it drops to ∼62.2% at 580 K. The simulation results agree with the observation that CO_2 is the dominant carbon source, for example, 91.9% from CO_2 on Zn-free Cu/MgO system (523 K, $CO/CO_2/H_2$ = 6/8/59, p_{tot} = 30 bar) by the isotope labeling experiment.[19] We also examine the TOF of methanol produced from CO_2 and CO at different CO_2 contents in the mixed gas ($p_{\mathrm{CO}} + p_{\mathrm{CO_2}}$ = 20 bar), which is plotted in Figure S12, and find that major source of methanol is CO_2 as long as the CO_2 content is larger than 8%.

Second, the presence of Zn in the CuZn alloy is beneficial at low Zn coverage (0.11 ML) above 540 K but slows the methanol synthesis in all other conditions. On 0.11 ML Zn−Cu(211), the CO_2 hydrogenation rate differs by no more than

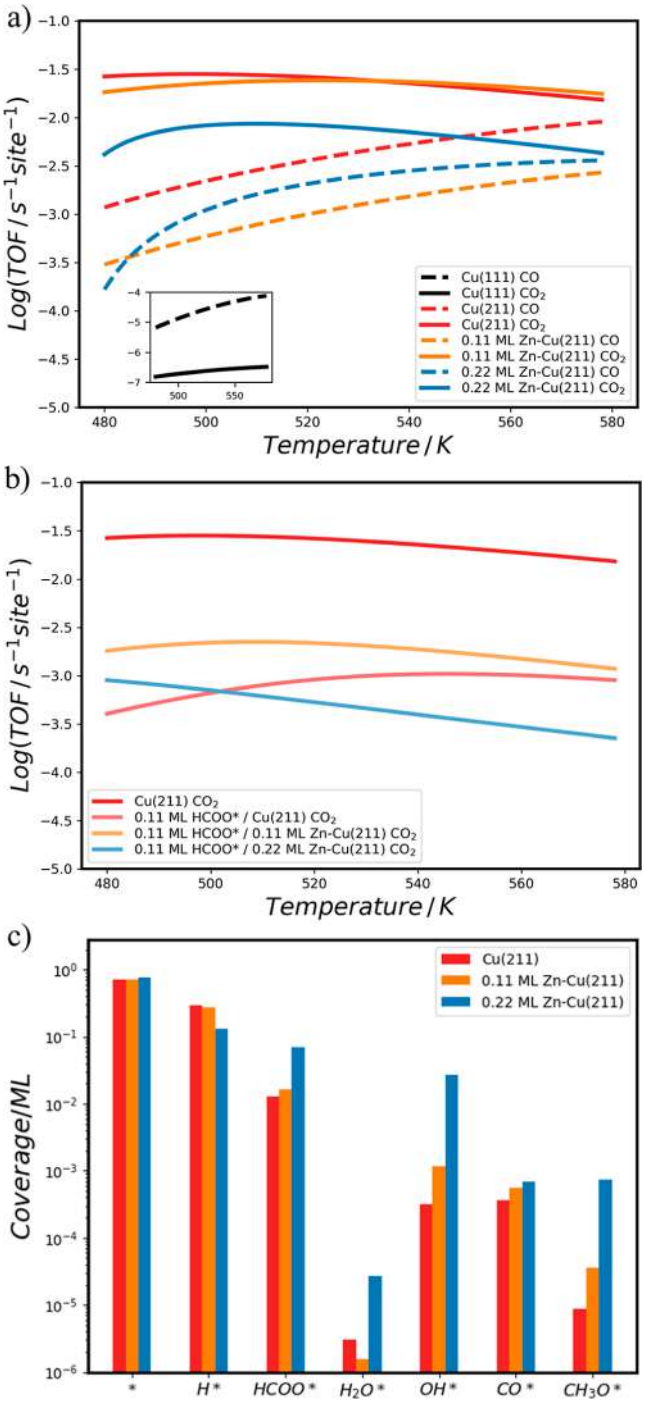

Figure 5. Microkinetics simulation results based on DFT energetics at typical reaction conditions, where pressures are 10, 10, 40, 1, and 1 bar for CO_2, CO, H_2, CH_3OH, and H_2O, respectively. The TOFs as a function of temperature at the steady state for (a) CO_2 and CO hydrogenations on Cu(111), Cu(211), 0.11 ML Zn−Cu(211), and 0.22 ML Zn−Cu(211) and for (b) CO_2 hydrogenation on HCOO* spectating Cu(211) surface and its Zn surface alloy. (c) Steady-state surface coverage of main species on Cu(211), 0.11 ML Zn−Cu(211), and 0.22 ML Zn−Cu(211) at 500 K.

1.5 times from that on Cu(211), being slower at low temperatures (<540 K) and higher at higher temperatures. However, on 0.22 ML Zn−Cu(211) (local Zn high coverage at step-edge), the CO_2 hydrogenation rate is several times slower compared to the rate without Zn. Focusing on the HCOOH*

https://doi.org/10.1021/jacs.2c06044
J. Am. Chem. Soc. 2022, 144, 13401−13414

+ H* step, we find that at 500 K, although the reaction rate constant of HCOOH* + H* on 0.22 ML Zn−Cu(211) (k_+ = 2.7 × 10^6 s^{-1}) is faster than that on Cu(211) (k_+ = 1.6 × 10^6 s^{-1}), both θ_{H^*} and θ_{HCOOH^*} (0.13 ML and 3.3 × 10^{-9} ML, respectively) are lower than those on Cu(211) (0.29 ML and 1.2 × 10^{-8} ML, respectively). It leads to 5 times lower forward reaction rate on 0.22 ML Zn−Cu(211) (r_+ = 1.0 × 10^{-2} s^{-1}) compared with clean Cu(211), and thus CO_2 hydrogenation on 0.22 ML Zn−Cu(211) has a TOF of 9.7 × 10^{-3} s^{-1} and is 2.9 times lower than that on clean Cu(211).

Third, the presence of HCOO* spectators decreases the methanol formation rate for all catalysts studied, as shown in Figures 5b and S13. For example, Figure 5b shows that at 500 K, on 0.11 ML HCOO*-covered Cu(211), CO_2 and CO hydrogenation rates are only 6.6 × 10^{-4}, 3 × 10^{-5} s^{-1}, both being 2 orders of magnitude slower than those on clean Cu(211). A major reason for the slow kinetics on 0.11 ML HCOO*/Cu(211) is the high coverage of H_2O at the step-edge (Figures S11 and S14). Compared to Cu(211), 0.11 ML Zn−Cu(211) is less sensitive to the HCOO* poisoning, where the rate drops by ∼10 times in the presence of the HCOO* spectator at 500 K.

Figure 5c shows further the steady-state coverage of key intermediates on Cu and Zn−Cu(211) surfaces at 500 K. On Cu(211), the surfaces are mainly covered by H* [e.g., 0.29 ML at 500 K on Cu(211)], and the other species with relatively high coverage include HCOO* (0.013 ML) and CO* (3.7 × 10^{-4} ML). The low coverage of HCOO* suggests that the HCOO* poisoning does not actually occur. In fact, our microkinetics simulation based on the DFT data of 0.11 ML HCOO*-covered Cu(211) confirms that the HCOO* coverage cannot maintain at the present value of 0.11 ML (see Figure S14) but drops to 10^{-5} ML. The Zn alloying can also change the coverage of species, as plotted in Figure 5c, leading to lower coverage of H* and higher coverage of HCOO*. For example, the H* and HCOO* coverage is 0.13 and 0.064 ML on the 0.22 ML Zn−Cu(211) surface, respectively, which results in a lower TOF for the catalyst.

4. DISCUSSIONS ON THE ACTIVE SITE

By computing the thermodynamics of CuZn alloy formation, this work confirms the thermodynamics tendency in forming CuZn alloy under reaction conditions, where pure Cu and 0.11 ML Zn−Cu(211) are the most common catalysts at a wide range of experimental conditions. With further reaction pathways sampling on CuZn alloy surfaces, we find that the low Zn coverage (0.11 ML) at the (211) step provides a similar activity as pure Cu in CO_2 hydrogenation, but the higher Zn coverage (0.22 ML) poisons the catalyst. Indeed, a recent experiment by Frei et al.[67] reported a negative effect of CuZn alloy on methanol synthesis under industrial conditions, in which the higher content of CuZn alloy prepared by using the higher H_2 activating temperature shows a lower CH_3OH formation rate and a higher apparent activation energy.

Since our kinetics results for Cu and CuZn alloy surfaces do not support the beneficial role of Zn in the CZA catalyst (e.g., Cu/ZnO catalyst is more than 10 times higher than ZnO-free Cu/SiO_2 catalyst in the experiment[68]), it is natural to wonder what else might contribute to the high activity of CZA catalysts. Following the literature in the Introduction, we are now in a better position to rethink the other popular active site model, that is, the cationic Zn, including the ZnO overlayer on Cu surfaces and the zinc formate species.[69] However, compared to CuZn alloys, theoretical studies on the cationic Zn are still rather limited due to the lack of valid structure models. There were a few attempts to construct the likely structural models, including ZnO overlayer on Cu(111),[70−72] ZnO_x cluster on Cu(111),[73,74] and $Zn_xO_yH_z$ clusters on Cu(111).[14,75] As a representative, Kattel et al. proposed an interesting ZnOH model with a $Zn_6O_7H_7$ cluster on Cu(111) (Figure 6a) and obtained the TOF of 0.09 s^{-1} for methanol synthesis by DFT calculations and kMC simulation,[14] which is close to the experimental TOF.

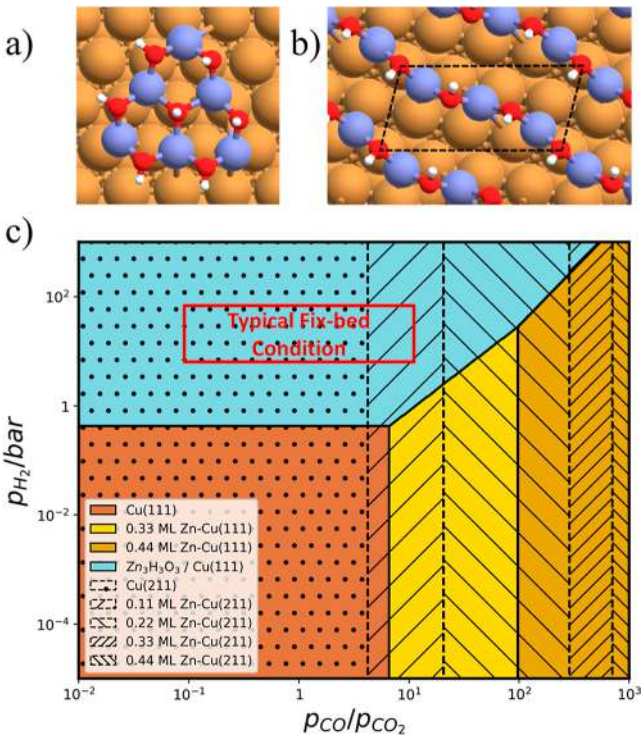

Figure 6. Structures of ZnOH overlayer on Cu(111) and the phase diagram of Cu−Zn catalyst after considering the ZnOH overlayer structure. (a) Model proposed previously by Kattel et al.;[14] (b) global minimum identified in this work. The color scheme for atoms is as follows: H: white; O: red; Cu: yellow; and Zn: blue. (c) Thermodynamics phase diagram of Cu−Zn catalyst at 500 K by considering both the CuZn alloy and the ZnOH overlayer. The thermodynamics stability of the surface at various H_2 pressures and CO/CO_2 pressures (p_{CO}/p_{CO_2}) is described by the formation free energy, explained in Supporting Information, Section 3. Color area for (111) and shaded area for (211) are overlapped in one plot, which shows that the ZnOH overlayer on (111) is present together with Cu(211) and 0.11 ML Zn−Cu(211) under typical reaction conditions.

Inspired by these previous works, we also utilize the SSW-NN method to explore the likely $Zn_xO_yH_z$ structures on different supercells of Cu(111), $Zn_xO_yH_z$/Cu(111), with variable x, y, and z compositions[76] (Zn coverage is ≤ 1 ML). Interestingly, the structure proposed by Kattel et al.[14] (Figure 6a) is in fact not the most stable structure. From our simulation, the global minimum configuration is a $Zn_3O_3H_3$ composition on a Cu(111) $p(\sqrt{13} \times \sqrt{3})$ supercell with the matrix notation (31 − 12), as shown in Figure 6b. This GM has a structure pattern of [−Zn−OH−Zn−] chains, where each Zn cation is linked by two OH groups and sits at the

https://doi.org/10.1021/jacs.2c06044
J. Am. Chem. Soc. 2022, 144, 13401−13414

hollow site of Cu(111). Under the reaction condition, this chain structure is 0.042 eV more stable per Cu(111) $p(1 \times 1)$ unit cell with respect to ZnO bulk, Cu(111), and H_2 (500 K, 10 bar CO and CO_2, 40 bar H_2, see Supporting Information, Section 3 for the chemical potential of O) (c.f. the structure proposed by Kattel et al. is 0.050 eV less stable per Cu(111) $p(1 \times 1)$ unit cell than the GM). The Bader charge analysis shows that the Zn in the chain structure is cationic, +0.76 to 0.78 |e|, but is less positively charged than Zn in ZnO (+1.19 |e|).

By combining with the thermodynamics data on CuZn alloys, we can now update the Cu−Zn phase diagram in Figure 6c (see Supporting Information, Section 3 for details on computing the thermodynamics). Apparently, Cu(211), 0.11 ML Zn−Cu(211) alloys, and the ZnOH overlayer structure are the three stable phases under reaction conditions where the partial pressure of H_2 exceeds ∼1 bar.

Our results imply that the Cu−ZnO catalyst structure is dynamic under different H_2, CO, and CO_2 pressure conditions, which can be utilized to understand the puzzling observations in the experiment. For example, ex situ TEM reveals the ZnO_x overlayer on the Cu surface for the H_2-activated catalyst,[11,13] which differs from the observations of only clean Cu surfaces without ZnO_x overlayer by in situ TEM at 1 mbar H_2, 300 °C[12] or at UHV condition.[77] From our results, the insufficient H_2 pressure in the in situ experiments cannot lead to the formation of the ZnO_x overlayer (see Figure 6c), where the ZnO_x overlayer must stem from the ZnOH ([−Zn−OH−Zn−]) precursor thin layer that is stable above a certain H_2 pressure (1 bar). The H_2 acts as the carrier to move oxidized Zn in ZnO to partially reduced Zn (ZnOH) on Cu surfaces.

Beck et al.[78] recently reported that during temperature-programmed reduction (25−500 °C), Zn K-edge X-ray absorption near-edge structure signal hardly changes at $p_{H_2} \leq$ 100 mbar but changes more pronouncedly when p_{H_2} exceeds 1 bar, indicating that H_2 pressure is critical for the structure evolution of Zn, as also suggested by us in Figure 6c. In their catalysis experiment, only independent CO_2 hydrogenation was investigated for methanol synthesis, from which they concluded that the CuZn alloy does not form to a large extent and is thus not the key active component. We would like to emphasize that the active site identified in this work can be both Cu steps and low-Zn content CuZn alloy steps (Figure 5a), and therefore, the lack of CuZn alloy in the pure CO_2 hydrogenation does not rule out the Cu steps being the active site since metallic Cu is always a dominant component in the CZA catalysts. In addition, the copresence of CO, as commonly utilized in the industry for methanol synthesis on CZA catalysts, is known to be critical to the overall methanol production activity. The presence of CO can further promote the CuZn alloy formation at surface steps from our results, as shown in Figure 2b, where the chemical potential of O is controlled via the ratio of CO and CO_2 (p_{CO}/p_{CO_2}).

Based on the results from this work and the knowledge from the previous work,[10,12,14,79−81] we propose the following picture for the CZA catalyst structure. Obviously, the catalyst structure dynamically evolves under catalytic conditions: ZnO close to the Cu/ZnO interface can be partially reduced by H_2 and migrates to Cu surfaces in forming the more stable [−Zn−OH−Zn−] overlayer structure at high H_2 pressures (e.g., the calcination stage of catalyst). These structures can be further reduced by CO or H_2 in the feed gas to form the CuZn surface alloy. In the meantime, the Zn atoms on Cu surfaces can also be reverted back to the [−Zn−OH−Zn−] overlayer and even a thicker ZnO_x overlayer by oxidative adsorbates generated during methanol synthesis (e.g., OH*, H_2O*, HCOO*, etc.).

The essentiality of H in the [−Zn−OH−Zn−] overlayer structure appears to be critical for understanding why H_2 is widely used to activate catalysts instead of using other reducing agents such as CO alone. We expect that the [−Zn−OH−Zn−] chain structure may serve as a precursor state of ZnO_x overlayer on Cu surfaces, which can effectively protect small Cu nanoparticles from sintering. On the other hand, as for the role of CO, a suitable window of CO/CO_2 ratio is critical for forming the low-Zn content CuZn surface alloy steps (Figure 2b), where the Zn helps to stabilize the stepped sites and thus facilitate CO_2 hydrogenation to methanol. Low CO pressure could lead to the Cu metal sites covered by [−Zn−OH−Zn−] overlayer structures and thus decrease the overall activity. Therefore, despite CO being much less active than CO_2 in hydrogenation, CO is required to expose more metallic Cu and ZnCu step-edges under reaction conditions. Further work is still needed to clarify the structure evolution of cationic Zn during methanol synthesis on CZA catalysts.

5. CONCLUSIONS

To recap, this work combines machine learning atomic simulation, thermodynamics analysis of surface structures, and automated reaction pathway identification to resolve the long-standing puzzles on the mixed gas CO_2/CO hydrogenation to methanol on Cu and CuZn surfaces. In particular, we develop a microkinetics-guided machine learning reaction pathway search method (MMLPS) for automated reaction pathway identification. The MMLPS method incorporates SSW-RS pathway exploration, a fast pathway filter, and a microkinetics solver. It utilizes the idea of divide-and-conquer to solve a complex reaction network with many intermediates and different surface coverages. Our main conclusions are highlighted as follows.

(i) CuZn alloy surfaces are thermodynamically favorable under methanol synthesis conditions (in the presence of CO and H_2), but the Zn coverage is limited to 1/3 ML on Cu(111) and 2/9 ML on Cu(211). The presence of CO helps to form the CuZn surface alloy that occurs preferentially at the step-edge site. In addition to the CuZn metal alloy at the step-edge, ZnOH overlayer on Cu surface is also likely to form above H_2 pressure 1 bar, which has a [−Zn−OH−Zn−] chain pattern with each OH being two-coordinated with nearby Zn. These Zn are cationic with +0.76 to 0.78 |e|. The CZA catalyst structure is thus dynamic under reaction conditions controlled by H_2, CO, and CO_2 pressures.

(ii) The kinetically favorable pathway for CO_2 hydrogenation follows the formate mechanism (CO_2−HCOO*−HCOOH*−H_2COOH*−HCHO*−CH_3O*−CH_3OH*) and that for CO hydrogenation follows the formyl mechanism (CO*−CHO*−HCHO*−CH_3O*−CH_3OH*). For CO_2 hydrogenation, both HCOO* formation and H_2COOH* formation are kinetically important and have similar overall free-energy barriers. For CO hydrogenation, it is the HCHO* formation that determines the overall free energy of methanol synthesis.

(iii) From microkinetics, the TOF of methanol synthesis at 500 K for CO_2 hydrogenation is 2.8×10^{-2} s^{-1} on Cu(211), much faster than that of CO hydrogenation (2.2×10^{-3}). Only at the high coverages of Zn, that is, 0.22 ML, does the TOF

https://doi.org/10.1021/jacs.2c06044
J. Am. Chem. Soc. 2022, 144, 13401−13414

decrease substantially to 9.7×10^{-3} at 500 K. The active sites for methanol synthesis are thus metallic Cu and low-Zn content CuZn steps. The coverage of HCOO* is low (<0.07 ML), which suggests that the HCOO* poisoning does not actually occur.

■ CODE AVAILABILITY

The MMLPS code is openly available on the website (https://github.com/lasphub/MMLPS).

■ ASSOCIATED CONTENT

Supporting Information

The Supporting Information is available free of charge at https://pubs.acs.org/doi/10.1021/jacs.2c06044.

MMLPS; free-energy corrections; equations for constructing thermodynamics phase diagram; SSW-NN method and G-NN potential; GM structures for 0.44 ML Zn−Cu(211) and Zn−Cu(211); reaction pair database: the CVs for viewing and other information; Gibbs free energy of key species based on DFT energetics; comparison of reaction barriers with previous studies; reaction snapshots for key reaction steps on (Zn−)Cu(211); reaction profiles on Cu and CuZn surfaces with HCOO* spectator; and microkinetics simulation results (PDF)

XYZ coordinates for key reaction states (TXT)

■ AUTHOR INFORMATION

Corresponding Authors

Cheng Shang − *Collaborative Innovation Center of Chemistry for Energy Material, Shanghai Key Laboratory of Molecular Catalysis and Innovative Materials, Key Laboratory of Computational Physical Science, Department of Chemistry, Fudan University, Shanghai 200433, China; Shanghai Qi Zhi Institution, Shanghai 200030, China;* orcid.org/0000-0001-7486-1514; Email: cshang@fudan.edu.cn

Zhi-Pan Liu − *Collaborative Innovation Center of Chemistry for Energy Material, Shanghai Key Laboratory of Molecular Catalysis and Innovative Materials, Key Laboratory of Computational Physical Science, Department of Chemistry, Fudan University, Shanghai 200433, China; Shanghai Qi Zhi Institution, Shanghai 200030, China; Key Laboratory of Synthetic and Self-Assembly Chemistry for Organic Functional Molecules, Shanghai Institute of Organic Chemistry, Chinese Academy of Sciences, Shanghai 200032, China;* orcid.org/0000-0002-2906-5217; Email: zpliu@fudan.edu.cn

Authors

Yun-Fei Shi − *Collaborative Innovation Center of Chemistry for Energy Material, Shanghai Key Laboratory of Molecular Catalysis and Innovative Materials, Key Laboratory of Computational Physical Science, Department of Chemistry, Fudan University, Shanghai 200433, China*

Pei-Lin Kang − *Collaborative Innovation Center of Chemistry for Energy Material, Shanghai Key Laboratory of Molecular Catalysis and Innovative Materials, Key Laboratory of Computational Physical Science, Department of Chemistry, Fudan University, Shanghai 200433, China;* orcid.org/0000-0003-2147-2472

Complete contact information is available at: https://pubs.acs.org/10.1021/jacs.2c06044

Notes

The authors declare no competing financial interest.

■ ACKNOWLEDGMENTS

This work was supported by the National Key Research and Development Program of China (2018YFA0208600), the National Science Foundation of China (12188101, 22033003, 91945301, 91745201, 92145302, 22122301, and 92061112), and the Tencent Foundation for XPLORER PRIZE.

■ REFERENCES

(1) Ertl, G.; Burgess, D. R. Thermochemical Data. *Handbook of Heterogeneous Catalysis*; VCH: Weinheim, 1997.

(2) Kondrat, S. A.; Smith, P. J.; Wells, P. P.; Chater, P. A.; Carter, J. H.; Morgan, D. J.; Fiordaliso, E. M.; Wagner, J. B.; Davies, T. E.; Lu, L.; Bartley, J. K.; Taylor, S. H.; Spencer, M. S.; Kiely, C. J.; Kelly, G. J.; Park, C. W.; Rosseinsky, M. J.; Hutchings, G. J. Stable Amorphous Georgeite as a Precursor to a High-Activity Catalyst. *Nature* **2016**, *531*, 83−87.

(3) Klier, K. Catalytic Synthesis of Methanol from CO/H2IV. The Effects of Carbon Dioxide. *J. Catal.* **1982**, *74*, 343−360.

(4) Martin, O.; Mondelli, C.; Curulla-Ferré, D.; Drouilly, C.; Hauert, R.; Pérez-Ramírez, J. Zinc-Rich Copper Catalysts Promoted by Gold for Methanol Synthesis. *ACS Catal.* **2015**, *5*, 5607−5616.

(5) Martin, O.; Pérez-Ramírez, J. New and Revisited Insights into the Promotion of Methanol Synthesis Catalysts by CO2. *Catal. Sci. Technol.* **2013**, *3*, 3343.

(6) Martin, O.; Mondelli, C.; Cervellino, A.; Ferri, D.; Curulla-Ferré, D.; Pérez-Ramírez, J. Operando Synchrotron X-ray Powder Diffraction and Modulated-Excitation Infrared Spectroscopy Elucidate the CO2Promotion on a Commercial Methanol Synthesis Catalyst. *Angew. Chem.* **2016**, *128*, 11197−11202.

(7) Frost, J. C. Junction effect interactions in methanol synthesis catalysts. *Nature* **1988**, *334*, 577−580.

(8) Klier, K. Methanol Synthesis. In *Advances in Catalysis*; Eley, D. D., Pines, H., Weisz, P. B., Eds.; Academic Press, 1982; Vol. *31*, pp 243−313.

(9) Nakamura, J.; Choi, Y.; Fujitani, T. On the Issue of the Active Site and the Role of ZnO in Cu/ZnO Methanol Synthesis Catalysts. *Top. Catal.* **2003**, *22*, 277−285.

(10) Behrens, M.; Studt, F.; Kasatkin, I.; Kühl, S.; Hävecker, M.; Abild-Pedersen, F.; Zander, S.; Girgsdies, F.; Kurr, P.; Kniep, B.-L.; Tovar, M.; Fischer, R. W.; Nørskov, J. K.; Schlögl, R. The Active Site of Methanol Synthesis over Cu/ZnO/Al 2 O 3 Industrial Catalysts. *Science* **2012**, *336*, 893−897.

(11) Lunkenbein, T.; Schumann, J.; Behrens, M.; Schlögl, R.; Willinger, M. G. Formation of a ZnO Overlayer in Industrial Cu/ZnO/Al2O3Catalysts Induced by Strong Metal-Support Interactions. *Angew. Chem., Int. Ed.* **2015**, *54*, 4544−4548.

(12) Kuld, S.; Thorhauge, M.; Falsig, H.; Elkjaer, C. F.; Helveg, S.; Chorkendorff, I.; Sehested, J. Quantifying the Promotion of Cu Catalysts by ZnO for Methanol Synthesis. *Science* **2016**, *352*, 969−974.

(13) Lunkenbein, T.; Girgsdies, F.; Kandemir, T.; Thomas, N.; Behrens, M.; Schlögl, R.; Frei, E. Bridging the Time Gap: A Copper/Zinc Oxide/Aluminum Oxide Catalyst for Methanol Synthesis Studied under Industrially Relevant Conditions and Time Scales. *Angew. Chem.* **2016**, *128*, 12900−12904.

(14) Kattel, S.; Ramírez, P. J.; Chen, J. G.; Rodriguez, J. A.; Liu, P. Active sites for CO 2 hydrogenation to methanol on Cu/ZnO catalysts. *Science* **2017**, *355*, 1296−1299.

(15) Fujitani, T. Enhancement of the Catalytic Performance and Active Site Clarification of Cu/ZnO Based Catalysts for Methanol Synthesis by CO2 Hydrogenation. *J. Jpn. Petrol. Inst.* **2020**, *63*, 43−51.

(16) Kuld, S.; Conradsen, C.; Moses, P. G.; Chorkendorff, I.; Sehested, J. Quantification of Zinc Atoms in a Surface Alloy on Copper in an Industrial-Type Methanol Synthesis Catalyst. *Angew. Chem.* **2014**, *126*, 6051−6055.

(17) Fujitani, T.; Nakamura, I.; Uchijima, T.; Nakamura, J. The Kinetics and Mechanism of Methanol Synthesis by Hydrogenation of CO2 over a Zn-Deposited Cu(111) Surface. *Surf. Sci.* **1997**, *383*, 285−298.
(18) Studt, F.; Abild-Pedersen, F.; Varley, J. B.; Nørskov, J. K. CO and CO2 Hydrogenation to Methanol Calculated Using the BEEF-VdW Functional. *Catal. Lett.* **2013**, *143*, 71−73.
(19) Studt, F.; Behrens, M.; Kunkes, E. L.; Thomas, N.; Zander, S.; Tarasov, A.; Schumann, J.; Frei, E.; Varley, J. B.; Abild-Pedersen, F.; Nørskov, J. K.; Schlögl, R. The Mechanism of CO and CO2Hydrogenation to Methanol over Cu-Based Catalysts. *ChemCatChem* **2015**, *7*, 1105−1111.
(20) van Rensburg, W. J.; Petersen, M. A.; Datt, M. S.; van den Berg, J.-A.; van Helden, P. On the Kinetic Interpretation of DFT-Derived Energy Profiles: Cu-Catalyzed Methanol Synthesis. *Catal. Lett.* **2015**, *145*, 559−568.
(21) Yang, Y.; Mims, C. A.; Mei, D. H.; Peden, C. H. F.; Campbell, C. T. Mechanistic Studies of Methanol Synthesis over Cu from CO/CO2/H2/H2O Mixtures: The Source of C in Methanol and the Role of Water. *J. Catal.* **2013**, *298*, 10−17.
(22) Chinchen, G. C.; Denny, P. J.; Parker, D. G.; Spencer, M. S.; Whan, D. A. Mechanism of Methanol Synthesis from CO2/CO/H2 Mixtures over Copper/Zinc Oxide/Alumina Catalysts: Use Of14C-Labelled Reactants. *Appl. Catal.* **1987**, *30*, 333−338.
(23) Wu, P.; Yang, B. Significance of Surface Formate Coverage on the Reaction Kinetics of Methanol Synthesis from CO2 Hydrogenation over Cu. *ACS Catal.* **2017**, *7*, 7187−7195.
(24) Xu, D.; Wu, P.; Yang, B. Origin of CO2 as the main carbon source in syngas-to-methanol process over Cu: theoretical evidence from a combined DFT and microkinetic modeling study. *Catal. Sci. Technol.* **2020**, *10*, 3346−3352.
(25) Bourzutschky, J. A. B.; Homs, N.; Bell, A. T. Hydrogenation of CO2 and CO2/CO Mixtures over Copper-Containing Catalysts. *J. Catal.* **1990**, *124*, 73−85.
(26) Kang, P.-L.; Shang, C.; Liu, Z.-P. Glucose to 5-Hydroxymethylfurfural: Origin of Site-Selectivity Resolved by Machine Learning Based Reaction Sampling. *J. Am. Chem. Soc.* **2019**, *141*, 20525−20536.
(27) Chen, D.; Kang, P.-L.; Liu, Z.-P. Active Site of Catalytic Ethene Epoxidation: Machine-Learning Global Pathway Sampling Rules Out the Metal Sites. *ACS Catal.* **2021**, *11*, 8317−8326.
(28) Kang, P.-L.; Liu, Z.-P. Reaction Prediction via Atomistic Simulation: From Quantum Mechanics to Machine Learning. *iScience* **2021**, *24*, 102013.
(29) Kang, P.-L.; Shi, Y.-F.; Shang, C.; Liu, Z.-P. Artificial Intelligence Pathway Search to Resolve Catalytic Glycerol Hydrogenolysis Selectivity. *Chem. Sci.* **2022**, *13*, 8148−8160.
(30) Gao, C. W.; Allen, J. W.; Green, W. H.; West, R. H. Reaction Mechanism Generator: Automatic Construction of Chemical Kinetic Mechanisms. *Comput. Phys. Commun.* **2016**, *203*, 212−225.
(31) Li, M. M.-J.; Tsang, S. C. E. Bimetallic catalysts for green methanol production via CO2 and renewable hydrogen: a mini-review and prospects. *Catal. Sci. Technol.* **2018**, *8*, 3450−3464.
(32) Rangarajan, S.; Bhan, A.; Daoutidis, P. Language-Oriented Rule-Based Reaction Network Generation and Analysis: Description of RING. *Comput. Chem. Eng.* **2012**, *45*, 114−123.
(33) Gupta, U.; Vlachos, D. G. Learning Chemistry of Complex Reaction Systems via a Python First-Principles Reaction Rule Stencil (PReSt) Generator. *J. Chem. Inf. Model.* **2021**, *61*, 3431−3441.
(34) Gu, T.; Wang, B.; Chen, S.; Yang, B. Automated Generation and Analysis of the Complex Catalytic Reaction Network of Ethanol Synthesis from Syngas on Rh(111). *ACS Catal.* **2020**, *10*, 6346−6355.
(35) Laio, A.; Gervasio, F. L. Metadynamics: A Method to Simulate Rare Events and Reconstruct the Free Energy in Biophysics, Chemistry and Material Science. *Rep. Prog. Phys.* **2008**, *71*, 126601.
(36) Martínez-Suárez, L.; Siemer, N.; Frenzel, J.; Marx, D. Reaction Network of Methanol Synthesis over Cu/ZnO Nanocatalysts. *ACS Catal.* **2015**, *5*, 4201−4218.
(37) Laio, A.; Parrinello, M. Escaping Free-Energy Minima. *Proc. Natl. Acad. Sci. U.S.A.* **2002**, *99*, 12562−12566.
(38) Bolhuis, P.; Chandler, D.; Dellago, C.; Geissler, P. Transition Path Sampling: Throwing Ropes over Rough Mountain Passes, in the Dark. *Annu. Rev. Phys. Chem.* **2002**, *53*, 291−318.
(39) Wales, D. J. Discrete Path Sampling. *Mol. Phys.* **2002**, *100*, 3285−3305.
(40) Rogers, D.; Hahn, M. Extended-Connectivity Fingerprints. *J. Chem. Inf. Model.* **2010**, *50*, 742−754.
(41) Chen, J.-F.; Mao, Y.; Wang, H.-F.; Hu, P. Reversibility Iteration Method for Understanding Reaction Networks and for Solving Microkinetics in Heterogeneous Catalysis. *ACS Catal.* **2016**, *6*, 7078−7087.
(42) Fishtik, I.; Callaghan, C. A.; Datta, R. Reaction Route Graphs. I. Theory and Algorithm. *J. Phys. Chem. B* **2004**, *108*, 5671−5682.
(43) Fishtik, I.; Callaghan, C. A.; Datta, R. Reaction Route Graphs. II. Examples of Enzyme- and Surface-Catalyzed Single Overall Reactions. *J. Phys. Chem. B* **2004**, *108*, 5683−5697.
(44) Fishtik, I.; Callaghan, C. A.; Datta, R. Reaction Route Graphs. III. Non-Minimal Kinetic Mechanisms. *J. Phys. Chem. B* **2005**, *109*, 2710−2722.
(45) Kozuch, S. Steady State Kinetics of Any Catalytic Network: Graph Theory, the Energy Span Model, the Analogy between Catalysis and Electrical Circuits, and the Meaning of "Mechanism". *ACS Catal.* **2015**, *5*, 5242−5255.
(46) Kozuch, S.; Shaik, S. How to Conceptualize Catalytic Cycles? The Energetic Span Model. *Acc. Chem. Res.* **2011**, *44*, 101−110.
(47) Yen, J. Y. Finding the K Shortest Loopless Paths in a Network. *Manag. Sci.* **1971**, *17*, 712−716.
(48) Dijkstra, E. W. A. A note on two problems in connexion with graphs. *Numerische Mathematlk* **1959**, *1*, 269−271.
(49) Byrne, G. D.; Hindmarsh, A. C. A Polyalgorithm for the Numerical Solution of Ordinary Differential Equations. *ACM Trans. Math Software* **1975**, *1*, 71−96.
(50) Johansson, F.; others *Mpmath: A Python Library for Arbitrary-Precision Floating-Point Arithmetic* (Version 0.18), 2013.
(51) Chen, S.; Ma, S.; Liu, Z.-P. Zirconia-Supported ZnO Single Layer for Syngas Conversion Revealed from Machine-Learning Atomic Simulation. *J. Phys. Chem. Lett.* **2021**, *12*, 3328−3334.
(52) Ma, S.; Huang, S.-D.; Liu, Z.-P. Dynamic coordination of cations and catalytic selectivity on zinc-chromium oxide alloys during syngas conversion. *Nat. Catal.* **2019**, *2*, 671−677.
(53) Huang, S.-D.; Shang, C.; Kang, P.-L.; Zhang, X.-J.; Liu, Z.-P. LASP: Fast Global Potential Energy Surface Exploration. *Wiley Interdiscip. Rev.: Comput. Mol. Sci.* **2019**, *9*, No. e1415.
(54) Huang, S.-D.; Shang, C.; Zhang, X.-J.; Liu, Z.-P. Material Discovery by Combining Stochastic Surface Walking Global Optimization with a Neural Network. *Chem. Sci.* **2017**, *8*, 6327−6337.
(55) Huang, S.-D.; Shang, C.; Kang, P.-L.; Liu, Z.-P. Atomic Structure of Boron Resolved Using Machine Learning and Global Sampling. *Chem. Sci.* **2018**, *9*, 8644−8655.
(56) Kresse, G.; Furthmüller, J. Efficient iterative schemes forab initiototal-energy calculations using a plane-wave basis set. *Phys. Rev. B: Condens. Matter Mater. Phys.* **1996**, *54*, 11169−11186.
(57) Kresse, G.; Joubert, D. From Ultrasoft Pseudopotentials to the Projector Augmented-Wave Method. *Phys. Rev. B: Condens. Matter Mater. Phys.* **1999**, *59*, 1758−1775.
(58) Perdew, J. P.; Burke, K.; Ernzerhof, M. Generalized Gradient Approximation Made Simple. *Phys. Rev. Lett.* **1996**, *77*, 3865−3868.
(59) Tameh, M. S.; Dearden, A. K.; Huang, C. Accuracy of Density Functional Theory for Predicting Kinetics of Methanol Synthesis from CO and CO2 Hydrogenation on Copper. *J. Phys. Chem. C* **2018**, *122*, 17942−17953.
(60) Wellendorff, J.; Lundgaard, K. T.; Møgelhøj, A.; Petzold, V.; Landis, D. D.; Nørskov, J. K.; Bligaard, T.; Jacobsen, K. W. Density Functionals for Surface Science: Exchange-Correlation Model Development with Bayesian Error Estimation. *Phys. Rev. B: Condens. Matter Mater. Phys.* **2012**, *85*, 235149.
(61) Cao, K.; Füchsel, G.; Kleyn, A. W.; Juurlink, L. B. F. Hydrogen Adsorption and Desorption from Cu(111) and Cu(211). *Phys. Chem. Chem. Phys.* **2018**, *20*, 22477−22488.

(62) Zhang, X.-J.; Shang, C.; Liu, Z.-P. Pressure-Induced Silica Quartz Amorphization Studied by Iterative Stochastic Surface Walking Reaction Sampling. *Phys. Chem. Chem. Phys.* **2017**, *19*, 4725−4733.
(63) Kopač, D.; Likozar, B.; Huš, M. Catalysis of Material Surface Defects: Multiscale Modeling of Methanol Synthesis by CO2 Reduction on Copper. *Appl. Surf. Sci.* **2019**, *497*, 143783.
(64) Grabow, L. C.; Mavrikakis, M. Mechanism of Methanol Synthesis on Cu through CO2 and CO Hydrogenation. *ACS Catal.* **2011**, *1*, 365−384.
(65) Wang, S.; Jian, M.; Su, H.; Li, W. First-Principles Microkinetic Study of Methanol Synthesis on Cu(221) and ZnCu(221) Surfaces. *Chin. J. Chem. Phys.* **2018**, *31*, 284−290.
(66) Sun, X.; Wang, P.; Shao, Z.; Cao, X.; Hu, P. A First-Principles Microkinetic Study on the Hydrogenation of Carbon Dioxide over Cu(211) in the Presence of Water. *Sci. China: Chem.* **2019**, *62*, 1686−1697.
(67) Frei, E.; Gaur, A.; Lichtenberg, H.; Zwiener, L.; Scherzer, M.; Girgsdies, F.; Lunkenbein, T.; Schlögl, R. Cu−Zn Alloy Formation as Unfavored State for Efficient Methanol Catalysts. *ChemCatChem* **2020**, *12*, 4029−4033.
(68) Burch, R.; Golunski, S. E.; Spencer, M. S. The Role of Copper and Zinc Oxide in Methanol Synthesis Catalysts. *Faraday Trans.* **1990**, *86*, 2683.
(69) Zabilskiy, M.; Sushkevich, V. L.; Palagin, D.; Newton, M. A.; Krumeich, F.; van Bokhoven, J. A. The Unique Interplay between Copper and Zinc during Catalytic Carbon Dioxide Hydrogenation to Methanol. *Nat. Commun.* **2020**, *11*, 2409.
(70) Thang, H. V.; Tosoni, S.; Pacchioni, G. The Epitaxial Growth of ZnO Films on Cu(111) Surface: Thickness Dependence. *Appl. Surf. Sci.* **2019**, *483*, 133−139.
(71) Liu, X.; Luo, J.; Wang, H.; Huang, L.; Wang, S.; Li, S.; Sun, Z.; Sun, F.; Jiang, Z.; Wei, S.; Li, W.-X.; Lu, J. In Situ Spectroscopic Characterization and Theoretical Calculations Identify Partially Reduced ZnO1−x/Cu Interfaces for Methanol Synthesis from CO2. *Angew. Chem., Int. Ed.* **2022**, *61*, No. e202202330.
(72) Wang, S.-S.; Su, H.-Y.; Gu, X.-K.; Li, W.-X. Differentiating Intrinsic Reactivity of Copper, Copper-Zinc Alloy, and Copper/Zinc Oxide Interface for Methanol Steam Reforming by First-Principles Theory. *J. Phys. Chem. C* **2017**, *121*, 21553−21559.
(73) Reichenbach, T.; Walter, M.; Moseler, M.; Hammer, B.; Bruix, A. Effects of Gas-Phase Conditions and Particle Size on the Properties of Cu(111)-Supported ZnyOx Particles Revealed by Global Optimization and Ab Initio Thermodynamics. *J. Phys. Chem. C* **2019**, *123*, 30903−30916.
(74) Reichenbach, T.; Mondal, K.; Jäger, M.; Vent-Schmidt, T.; Himmel, D.; Dybbert, V.; Bruix, A.; Krossing, I.; Walter, M.; Moseler, M. Ab Initio Study of CO2 Hydrogenation Mechanisms on Inverse ZnO/Cu Catalysts. *J. Catal.* **2018**, *360*, 168−174.
(75) Li, D.; Xu, F.; Tang, X.; Dai, S.; Pu, T.; Liu, X.; Tian, P.; Xuan, F.; Xu, Z.; Wachs, I. E.; Zhu, M. Induced Activation of the Commercial Cu/ZnO/Al2O3 Catalyst for the Steam Reforming of Methanol. *Nat. Catal.* **2022**, *5*, 99−108.
(76) Chen, D.; Shang, C.; Liu, Z.-P. Automated Search for Optimal Surface Phases (ASOPs) in Grand Canonical Ensemble Powered by Machine Learning. *J. Chem. Phys.* **2022**, *156*, 094104.
(77) Hansen, P. L.; Wagner, J. B.; Helveg, S.; Rostrup-Nielsen, J. R.; Clausen, B. S.; Topsøe, H. Atom-Resolved Imaging of Dynamic Shape Changes in Supported Copper Nanocrystals. *Science* **2002**, *295*, 2053−2055.
(78) Beck, A.; Zabilskiy, M.; Newton, M. A.; Safonova, O.; Willinger, M. G.; van Bokhoven, J. A. Following the Structure of Copper-Zinc-Alumina across the Pressure Gap in Carbon Dioxide Hydrogenation. *Nat. Catal.* **2021**, *4*, 488−497.
(79) Laudenschleger, D.; Ruland, H.; Muhler, M. Identifying the Nature of the Active Sites in Methanol Synthesis over Cu/ZnO/Al2O3 Catalysts. *Nat. Commun.* **2020**, *11*, 3898.
(80) Divins, N. J.; Kordus, D.; Timoshenko, J.; Sinev, I.; Zegkinoglou, I.; Bergmann, A.; Chee, S. W.; Widrinna, S.; Karslıoğlu, O.; Mistry, H.; Lopez Luna, M.; Zhong, J. Q.; Hoffman, A. S.; Boubnov, A.; Boscoboinik, J. A.; Heggen, M.; Dunin-Borkowski, R. E.; Bare, S. R.; Cuenya, B. R. Operando High-Pressure Investigation of Size-Controlled CuZn Catalysts for the Methanol Synthesis Reaction. *Nat. Commun.* **2021**, *12*, 1435.
(81) Amann, P.; Klötzer, B.; Degerman, D.; Köpfle, N.; Götsch, T.; Lömker, P.; Rameshan, C.; Ploner, K.; Bikaljevic, D.; Wang, H.-Y.; Soldemo, M.; Shipilin, M.; Goodwin, C. M.; Gladh, J.; Halldin Stenlid, J.; Börner, M.; Schlueter, C.; Nilsson, A. The State of Zinc in Methanol Synthesis over a Zn/ZnO/Cu(211) Model Catalyst. *Science* **2022**, *376*, 603−608.

Recommended by ACS

Elucidation of Cu–Zn Surface Alloying on Cu(997) by Machine-Learning Molecular Dynamics

Harry H. Halim and Yoshitada Morikawa

JUNE 15, 2022
ACS PHYSICAL CHEMISTRY AU
READ

Selective Methane Oxidation to Methanol on $ZnO/Cu_2O/Cu(111)$ Catalysts: Multiple Site-Dependent Behaviors

Erwei Huang, Ping Liu, *et al.*

NOVEMBER 04, 2021
JOURNAL OF THE AMERICAN CHEMICAL SOCIETY
READ

Insights into the Selectivity Determinant and Rate-Determining Step of CO_2 Hydrogenation to Methanol

Chizhou Tang, Can Li, *et al.*

JUNE 16, 2022
THE JOURNAL OF PHYSICAL CHEMISTRY C
READ

Plasma-Catalytic Methanol Synthesis from CO_2 Hydrogenation over a Supported Cu Cluster Catalyst: Insights into the Reaction Mechanism

Zhaolun Cui, Annemie Bogaerts, *et al.*

JANUARY 07, 2022
ACS CATALYSIS
READ

Get More Suggestions >

https://doi.org/10.1021/jacs.2c06044
J. Am. Chem. Soc. 2022, 144, 13401−13414